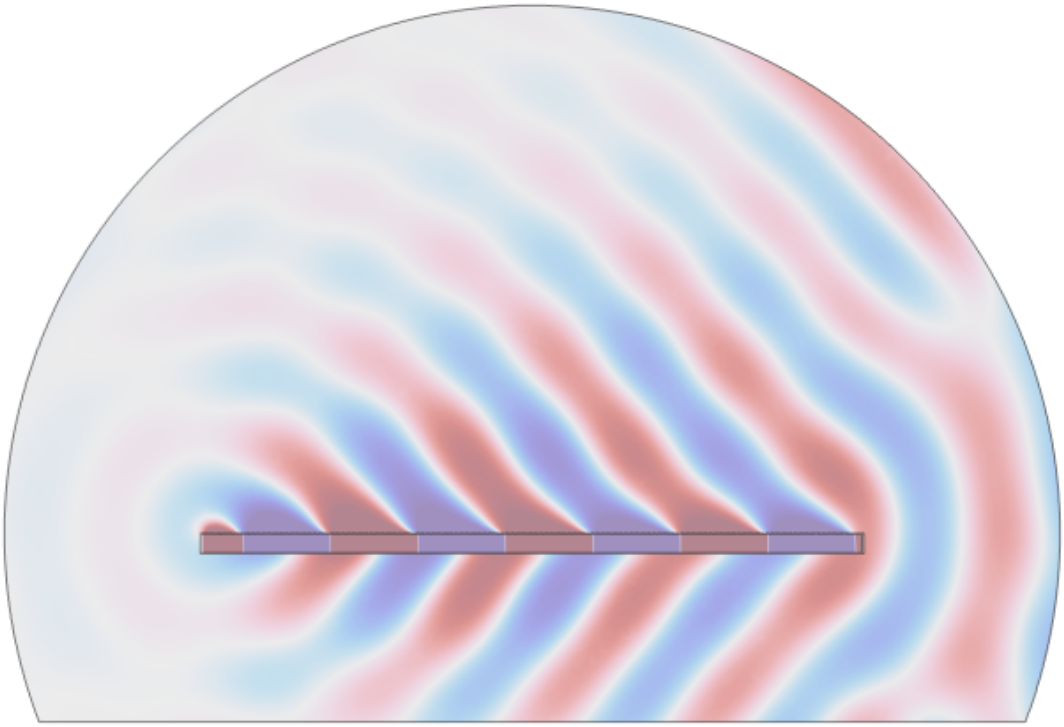

Designing a Prototype Acoustic Leaky Wave Antenna

Master's thesis in Sound and Vibration

MATTHEW POLIDANO

DEPARTMENT OF ARCHITECTURE AND CIVIL ENGINEERING

CHALMERS UNIVERSITY OF TECHNOLOGY
Gothenburg, Sweden 2025
www.chalmers.se

Master's thesis 2025

Designing a Prototype Acoustic Leaky Wave Antenna

MATTHEW POLIDANO

CHALMERS
UNIVERSITY OF TECHNOLOGY

Department of Architecture and Civil Engineering
Division of Applied Acoustics
Chalmers University of Technology
Gothenburg, Sweden 2025

Designing a Prototype Acoustic Leaky Wave Antenna

MATTHEW POLIDANO

Supervisor: Professor Jens Forssén, Applied Acoustics
Examiner: Professor Jens Forssén, Applied Acoustics

Master's Thesis 2025
Department of Architecture and Civil Engineering
Division of Applied Acoustics
Chalmers University of Technology
SE-412 96 Gothenburg
Telephone +46 31 772 1000

Cover: Visualisation of the sound pressure field of an Acoustic Leaky Wave Antenna simulated in COMSOL.

Typeset in LaTeX
Printed by Chalmers Reproservice
Gothenburg, Sweden 2025

Designing a Prototype Acoustic Leaky Wave Antenna
MATTHEW POLIDANO
Department of Architecture and Civil Engineering
Chalmers University of Technology

Abstract

Acoustic direction finding is a useful tool for navigational applications. Current techniques for achieving this rely on the use of many electro-acoustic components, which are expensive to produce and consume a lot of power. Acoustic Leaky Wave Antennas (ALWAs) offer a potential for a low-cost alternative, using much fewer electro-acoustic components and the inherent directionality of the geometrical structure to produce a similar effect. ALWAs possess a directionality which changes with frequency due to their dispersive properties, hence allowing for frequency scanning. Natural material ALWAs can scan angles from broadside (perpendicular to the length of the antenna) to endfire (parallel to the length of the antenna). Metamaterials may be used to extend the range to backfire (180° from endfire).

This thesis focuses on deriving a model for a rectangular natural material ALWA with either a long slit or a series of periodically spaced circular holes. The theoretical model was tested using Finite Element Method (FEM) simulations in Comsol and experimental measurements of a physical prototype. First, the theoretical model was tested with Comsol simulations. When the model was verified by the simulations, two particular designs with circular holes were chosen for the manufacture of physical prototypes. The directivity of the prototypes was measured using a rotating table and a microphone. Monopole and dipole sources were used to investigate different modes of the ALWA.

The results obtained for the ALWA with holes showed good agreement between the theoretical model, the FEM simulation and the experimental measurements. For the slit ALWA, the results were also satisfactory. However, the model may be improved, particularly at lower frequencies.

Keywords: Acoustic Leaky Wave Antenna, Frequency Scanning, Theoretical Model, Experimental Measurements, Finite Element Method Simulations.

Acknowledgements

I would like to thank those whose support was instrumental for the completion of this thesis.

First, I would like to thank my supervisor and examiner, Prof. Jens Forssén. His advice and support were critical for the development of this project. This thesis was done in collaboration with a student from the Universidad Politécnica de Cartagena, Pablo Antonio Martínez Vicente and his supervisors Dr. Astrid María Algaba Brazález and Prof. José Lius Gómez Tornero. They offered insight about Leaky Wave Antennas from the perspective of electromagnetics. I would also like to thank Sebastian Almfeldt and Sebastian Daniec who manufactured the physical ALWA prototypes, the loudspeaker fittings and the reflector termination.

I would like to acknowledge the financial assistance of the Endeavour II scholarship scheme and the ESF+ 2021-2027, who funded my studies at the Chalmers University of Technology as noted on the following page.

In addition, I would like to thank Logan Esser, who aided with proof-reading parts of this thesis and my opponent Valentin Quoniam Barré who challenged the ideas presented in this thesis and suggested improvements. Finally, I would like to acknowledge the support of my friends and family during my work on this project.

Matthew Polidano, Gothenburg, June 2025

GOVERNMENT
OF MALTA

FONDI.eu

The research work disclosed in this publication is partially funded by the Endeavour II Scholarships Scheme. The project is co-funded by the ESF+ 2021-2027

Co-funded by
the European Union

ENDEAVOUR
SCHOLARSHIPS SCHEME

List of Acronyms

Below is the list of acronyms that have been used throughout this thesis listed in alphabetical order:

ALWA	Acoustic Leaky Wave Antenna
CRLH	Composite Right/Left-Hand
FEM	Finite Element Method
FFT	Fast Fourier Transform
LWA	Leaky Wave Antenna
PMB	Perfectly Matched Boundary
PML	Perfectly Matched Layer
SPL	Sound Pressure Level
TEN	Transfer Equivalent Network
TL	Transmission Line
TRE	Transfer Resonance Equation

Contents

List of Figures

List of Tables

1

Introduction

Acoustic waves have useful properties for navigation. One such classical application is echolocation, used by some animals such as bats, wherein the time delay between the emission of a sound and the arrival of its reflection can be used to determine the distance between the source and the object which scatters the sound. However, it is not possible to obtain information about the direction to an object from a single omnidirectional source-receiver pair. To achieve this, one must either use multiple receiver-source pairs or a structure with an inherent directionality [1].

Current acoustic localization applications typically use microphone arrays, which use array processing that applies phase delays such that the desired directivity is obtained. This technique is complex and requires multiple components; hence, research is being conducted on Acoustic Leaky Wave Antennas (ALWAs) as a potential alternative for acoustic localization applications with size and energy constraints [1]. Achieving acoustic direction finding with less components would lead to lower-cost and more sustainable designs, further incentivizing the use of acoustic antennas for various applications.

1.1 Research Aim

This study aims to determine a theoretical model for the design of rectangular natural material ALWAs. The model considers ALWA designs with either a slit or periodically spaced circular holes as the radiating orifice. The two lowest frequency modes of the ALWA are considered in this study.

The developed theoretical model is tested using Finite Element Method (FEM) simulations and experimental measurements of physical prototypes. The results of these methods are then compared to assess the validity of the theoretical model.

This study is performed as a basis for researching the possibility of modulating the radiation properties of an ALWA along its length. By characterizing the behavior of the ALWA with different combinations of dimensions of the cavity and radiating orifices, future studies on modulation become possible.

1.2 Research Questions

The main questions this study seeks to answer are as follows.

- Is it possible to create a theoretical model which can describe the behavior of a rectangular natural-material ALWA?
- Can the model make accurate predictions of the properties of ALWAs with different dimensions when validated by FEM simulations?
- Can a physical prototype be manufactured that demonstrates the properties predicted by the theoretical model and/or the FEM simulations?

1.3 Structure of this Thesis

This thesis is structured in four further chapters as follows:

Chapter 2: Theory describes the relevant background information required to understand ALWA physics. The theory developed for the characterization of rectangular ALWAs is derived and presented in this section. A brief summary of research on metamaterial ALWAs and ALWA applications is also presented.

Chapter 3: Methodology describes the procedure used to calculate a numerical solution of the theoretical model, the set-up of the FEM simulations and the method used for the experimental measurements. A detailed overview of the manufacturing process of the prototypes and the measurement set-up is provided.

Chapter 4: Results and Discussion shows the results of the theoretical model compared to the FEM simulation and experimental measurements. Plots of the variation of the key design parameters with frequency are shown for different dimensions of the ALWA cavity and radiating orifice. Other useful plots, such as directivity plots and sound pressure surface plots are also presented and discussed.

Chapter 5: Conclusion summarizes the findings of this study and discusses its limitations. Suggestions for further research are given.

Appendix A introduces a proposal for an extension of the theoretical model to include a Helmholtz resonator.

2

Theory

This chapter discusses the background information and theory needed to understand Acoustic Leaky Wave Antennas (ALWAs). The theoretical model for rectangular natural material ALWAs is derived in this chapter, including a description of the impedance of a long slit and a series of circular holes as required for the calculation of the model. Finally, a summary of metamaterial ALWAs and applications of ALWAs is given.

2.1 Historical Overview

The concept of a Leaky Wave Antenna (LWA) first emerged for electromagnetic applications in the 1940s, when a patent was filed for an antenna consisting of a slotted waveguide with a suggested application in aviation [2]. Research on LWAs stalled until the 1950s, when several different designs and methods of analysis were proposed [3]. Many of the initial designs used a continuous slit in a waveguide to generate radiation. However, this design could not create sufficiently narrow beams due to the effects of the perturbations in the electric field caused by the slit [3]. As a solution, Hines and Upson proposed a LWA design with a series of closely spaced holes instead of the continuous slit allowing for narrow beam radiation [3]. The introduction of metamaterials has further increased the interest in the research of LWAs, allowing for the introduction of novel designs such as the CRLH (Composite Right/Left-Handed) LWA [4]. This design uses metamaterial properties to achieve continuous scanning from the backward quadrant to the forward quadrant [4].

The success of the LWA in electromagnetism was sought to be replicated for acoustic applications. In 2010, Bongard et al. [5] proposed a design for a Transmission Line (TL) based acoustic metamaterials using unit cells composed of membranes and open channels. With this design, it was theoretically possible to achieve a negative refractive index band as well as a zero index frequency. In 2013, Naify et al. [6] realized an Acoustic Leaky Wave Antenna (ALWA) using this metamaterial design and tested it with simulations and experimental measurements. This ALWA demonstrated the ability to radiate sound in the direction normal to the antenna and at angles on both sides of the normal.

Following the initial success of Naify et al., more studies have been conducted on ALWAs for different applications, including acoustic dispersive prisms [7] and single microphone direction finding [8]. Other studies have also investigated ALWAs for underwater applications [9, 10].

2.2 ALWA Physical Principles

2.2.1 Acoustic Waveguides

In a cavity, sound waves can form standing wave patterns in a number of modes. A waveguide is a cavity which is open in one or two of the dimensions. The rigid walls of the waveguide impose the condition that the particle velocity normal to the walls is zero. For a rectangular waveguide that is open in the z-dimension, the wave equation solution with these boundary conditions is [11]

$$\begin{aligned} p_{nm} &= A_{nm}\cos\left(k_{xn}x\right)\cos\left(k_{ym}y\right)e^{j(\omega t - k_z z)} \\ k_z &= \left[\left(\frac{\omega}{c}\right)^2 - \left(k_{xn}^2 + k_{ym}^2\right)\right]^{\frac{1}{2}} \\ k_{xn} &= \frac{n\pi}{W}, \qquad n = 0, 1, 2, \ldots \\ k_{ym} &= \frac{m\pi}{H}, \quad m = 0, 1, 2, \ldots \end{aligned} \tag{2.1}$$

where A_{nm} is the amplitude of the mode (n,m), W and H are the lengths of the cavity in the x and y dimensions respectively, ω is the angular frequency and c is the speed of sound. The terms labeled k represent the wavenumbers, in the axis and mode specified by the subscript. The waves can propagate inside the waveguide in various modes with different combinations of values of n and m.

Consider the expression for k_z; if $k_0 = \frac{\omega}{c}$ is larger than $k_{nm} = \sqrt{k_{xn}^2 + k_{ym}^2}$, then the value of k_z is real. In this case, the wave propagates in the $+z$ direction and is called a propagating mode. The frequency below which k_z is no longer real is called the cut-off frequency of the mode (n,m) and is given by [11]:

$$\omega_{nm} = ck_{nm} = c\sqrt{k_{xn}^2 + k_{ym}^2} \tag{2.2}$$

If the frequency is below the cut-off frequency for a given mode, the exponential term in the pressure equation becomes an exponential decay. This is called an evanescent wave and decays with distance inside the waveguide. Hence, if the waveguide is excited by a certain driving frequency, all modes with a cut-off frequency below the driving frequency will propagate in the waveguide, but all modes with a cut-off frequency higher than the driving frequency will be evanescent [11].

2.2.2 Leaky Waves

Putting a slit on one of the waveguide walls parallel to the z-direction allows some waves to leak and radiate to the outside. For an ALWA with a sound source placed inside, the pressure field of the radiated waves has the form [8, 12]

$$p(x, z) = p_0 e^{-jk_x x} e^{-jk_z z} e^{j\omega t} \tag{2.3}$$

where z is the direction of propagation of the traveling waves in the ALWA, x is the direction normal to the slit and k_x and k_z are the propagation constants in the x and z directions respectively, as shown in Figure 2.1.

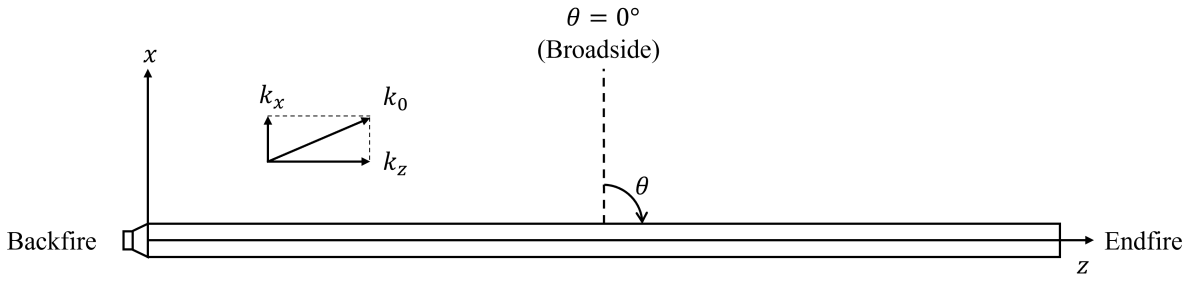

Figure 2.1: Defining the directions for the ALWA.

The wave number k_z, will in general be complex and can be defined as $k_z = \beta - j\alpha$ [12], where α and β are the leakage factor and the propagation constant, respectively. The wavenumber components in the orthogonal directions are related by [11]

$$k_0 = \sqrt{k_x^2 + k_y^2 + k_z^2} \implies k_z = \sqrt{k_0^2 - k_x^2 - k_y^2} \tag{2.4}$$

Now, since the waveguide is closed in the y-direction and the frequency of operation of the ALWA is here assumed to be less than the cut-off of the first mode in this direction, whereby:

$$k_y = 0 \quad \text{and} \quad k_z = \sqrt{k_0^2 - k_x^2}. \tag{2.5}$$

If $\alpha \ll 1$, the propagation constant k_x can be approximated by the expression [8]:

$$k_x \approx \sqrt{k_0^2 - \beta^2}. \tag{2.6}$$

This equation gives rise to two distinct cases. If $\beta > k_0$, then k_x is purely imaginary and there is no radiation, that is, the wave is guided in the waveguide. If $|\beta| < k_0$, k_x becomes real and radiation occurs, that is, the wave is a leaky wave. [8, 13]

2.2.3 ALWA Fundamental Parameters

The real and imaginary parts of k_z are the two fundamental parameters for designing an LWA and hence, also for an ALWA[13].

The Propagation Constant

The real part β is the propagation constant which determines the angle of radiation. The angle of radiation can be calculated in terms of the propagation constant as [8, 12, 13]

$$\theta_r = \sin^{-1}\left(\frac{\beta}{k_0}\right). \tag{2.7}$$

Furthermore, the half-power bandwidth of the main lobe can be approximated as [12, 13]:

$$\Delta\theta \approx \frac{\lambda}{L\cos(\theta_r)} \tag{2.8}$$

where L is the length of the antenna.

The Leakage Factor

The imaginary part α is the leakage factor which determines the amount of radiation per unit length [13]. In the case of a lossless ALWA with no reflection at the end of the antenna, the leakage factor can be calculated from [8]

$$\Psi_2 = \Psi_1 e^{-2\alpha l_{12}} \implies \alpha = \frac{1}{2l_{12}} \ln\left(\frac{\Psi_1}{\Psi_2}\right) \tag{2.9}$$

where Ψ_1 and Ψ_2 are the average power through an interior cross-section of the ALWA separated by a distance l_{12}.

The radiation efficiency of an ALWA can be calculated as [8]:

$$\eta_{rad} = 1 - e^{-2\alpha L}. \tag{2.10}$$

Hence, the length of the ALWA needed to achieve a radiation efficiency of e.g. 90% is [8]

$$\frac{L}{\lambda_0} \approx \frac{0.18}{\alpha/k_0}. \tag{2.11}$$

Decomposing the leakage factor into active and reactive parts

Using complex-valued powers, the leakage factor can be divided into two parts to describe the attenuation of the real (active) and imaginary (reactive) components. The active attenuation is associated with the radiated power and material losses while the reactive attenuation is related to energy storage. Reactive power is associated with power that is reflected back to the source instead of being delivered to the antenna and contributing to the leaky wave radiation [14, 15].

The instantaneous acoustic power in a cross-section of the ALWA cavity can be calculated for a single-frequency sound field as [16]

$$\Psi = \int_S \mathbf{I}_c \cdot \hat{\mathbf{z}}\, dS \qquad \mathbf{I}_c = \frac{1}{2} p \mathbf{u}^* \tag{2.12}$$

where S is the surface of the cross-section of the ALWA lying on the x-y-plane, $\hat{\mathbf{z}}$ is the unit vector in the z-direction, $I_c(x, y)$ is the instantaneous complex intensity, p is the complex pressure, $\mathbf{u}$ is the complex velocity and * denotes the complex conjugate. When the time-average of I_c is taken, the imaginary part vanishes, leaving only the contribution of the active intensity [16].

Now, from the definition of the specific acoustic impedance:

$$Z_{0,z} = \frac{p}{\mathbf{u} \cdot \hat{\mathbf{z}}} = \frac{\rho_0 \omega}{k_z} \implies \mathbf{u}^* \cdot \hat{\mathbf{z}} = \frac{p^* k_z^*}{\rho_0 \omega} = \frac{p^* (\beta + j\alpha)}{\rho_0 \omega}. \tag{2.13}$$

Therefore the instantaneous power at the source can be calculated as

$$\Psi(0) = \frac{1}{2} \int_S \frac{|p|^2 (\beta + j\alpha)}{\rho_0 \omega}\, dS = \frac{(\beta + j\alpha)}{2\rho_0 \omega} \int_S |p|^2\, dS \tag{2.14}$$

From Eq. (2.9), the power at the distance z from the source can be expressed as [15]

$$\Psi(z) = \Psi(0)e^{-2\alpha z} = |\Psi(0)|e^{-2\alpha z}e^{j\phi} \tag{2.15}$$

where $\phi = \arctan\left(\frac{\alpha}{\beta}\right)$ and $|\Psi(0)|$ are the phase and magnitude of the complex power at the source respectively, obtained from Eq. (2.14).

The leakage factor can be found by differentiating the power with respect to z as follows [15]:

$$-\frac{\mathrm{d}\Psi(z)}{\mathrm{d}z} = 2\alpha|\Psi(0)|e^{-2\alpha z}e^{j\phi} = 2\alpha e^{j\phi}|\Psi(z)| = 2\alpha|\Psi(z)|\left(\cos(\phi) + j\sin(\phi)\right). \tag{2.16}$$

Separating this into its real and imaginary components, we obtain the active and reactive components [14]:

$$\alpha_{\text{act}} = \frac{\text{Re}\left[-\frac{\mathrm{d}\Psi(z)}{\mathrm{d}z}\right]}{2|\Psi(z)|} = \alpha\cos(\phi), \qquad \alpha_{\text{react}} = \frac{\text{Im}\left[-\frac{\mathrm{d}\Psi(z)}{\mathrm{d}z}\right]}{2|\Psi(z)|} = \alpha\sin(\phi). \tag{2.17}$$

2.3 Natural Material Rectangular ALWA Designs

A simple design of a uniform ALWA is a rectangular waveguide with a slit on one side. The cross-section of such an ALWA design is shown in Figure 2.2. The direction of propagation of the waves in the ALWA is the z-direction, which extends perpendicular to the xy-plane. The source is located at one end of the ALWA ($z = 0$) and at the opposite end ($z = L$) an absorber is placed, such that no waves are reflected back. The length of the ALWA in the z-direction is L, which must be significantly larger than the wavelength of the lowest operating frequency. A quasi-uniform design can also be made by replacing the slit with a series of periodically spaced circular holes, with a period $b \ll \lambda$ [17].

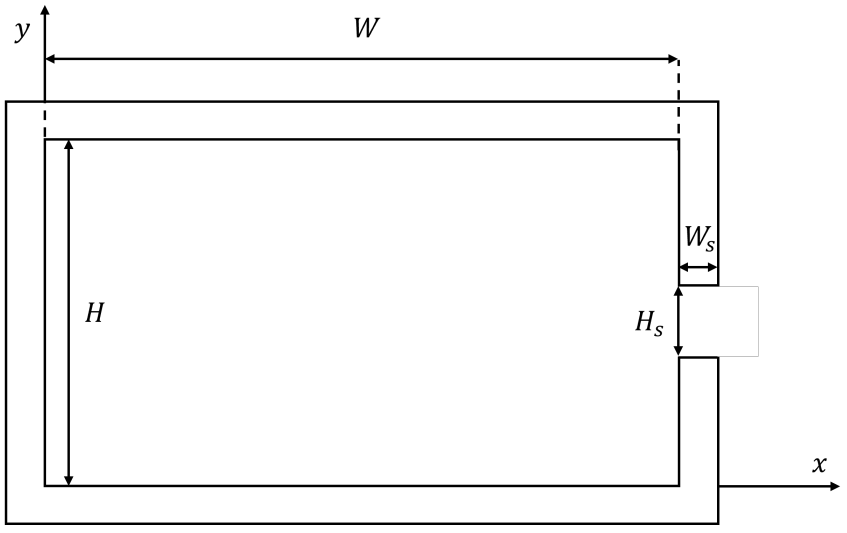

Figure 2.2: The cross-section of a Uniform Rectangular ALWA.

Now, to obtain an expression for the ALWA design parameters, we must solve a Transfer Resonance Equation (TRE) for the Transfer Equivalent Network in the x-direction, TEN_x, hence obtaining the value of k_x, which can be used to find k_z.

2.3.1 Deriving and Solving the Transfer Resonance Equation

The pressure of the sound waves in the x-direction of the ALWA as shown in Figure 2.2 can be modeled as a linear combination of harmonic waves traveling in the positive and negative directions, that is [11]:

$$p(x,t) = Ae^{j[\omega t + k_x(W-x)]} + Be^{j[\omega t - k_x(W-x)]} \tag{2.18}$$

where k_x is the wavenumber of the ALWA in the x-direction, and A and B are the amplitudes of the forwards and backwards traveling waves respectively.

The velocity is related to the pressure by [11]:

$$u(x,t) = -\frac{1}{\rho_0}\int \frac{\partial p}{\partial x}\,dt = -\frac{1}{j\omega\rho_0}\cdot\frac{\partial p}{\partial x} = \frac{1}{\omega\rho_0}\left[Ak_x e^{jk_x(W-x)} - Bk_x e^{-jk_x(W-x)}\right]e^{j\omega t}. \tag{2.19}$$

The specific acoustic impedance is defined as the ratio of the pressure and the velocity, that is, $Z = \frac{p(x,t)}{u(x,t)}$. Let $x = 0$ be the position of the left internal wall of the ALWA cavity and $x = W$ be the position of the internal wall of the ALWA cavity that contains the radiating orifice. Suppose that the impedances of the left and right walls are Z_L and Z_R, respectively. Then these boundary conditions can be used to find the amplitudes A and B as follows:

$$\begin{aligned} \text{At } x = 0: \qquad & Z_L = \frac{p(0,t)}{u(0,t)} = \frac{\omega\rho_0}{k_x}\cdot\frac{\left(Ae^{jk_xW} + Be^{-jk_xW}\right)\cancel{e^{j\omega t}}}{\left(Ae^{jk_xW} - Be^{-jk_xW}\right)\cancel{e^{j\omega t}}} \\ \text{At } x = W: \qquad & Z_R = \frac{p(W,t)}{u(W,t)} = \frac{\omega\rho_0}{k_x}\cdot\frac{(A+B)\cancel{e^{j\omega t}}}{(A-B)\cancel{e^{j\omega t}}} \end{aligned} \tag{2.20}$$

Let $Z_{0,x} = \rho_0\omega/k_x$ represent the characteristic impedance of the ALWA in the x-direction. Then,

$$\begin{aligned} Z_R = Z_{0,x}\cdot\frac{A+B}{A-B} \implies A = B\cdot\frac{Z_R + Z_{0,x}}{Z_L - Z_{0,x}} \\ \text{and } Z_L = Z_{0,x}\cdot\frac{B\frac{Z_R+Z_{0,x}}{Z_L-Z_{0,x}}e^{jk_xW} + Be^{-jk_xW}}{B\frac{Z_R+Z_{0,x}}{Z_L-Z_{0,x}}e^{jk_xW} - Be^{-jk_xW}} \end{aligned} \tag{2.21}$$

$$\implies Z_L = \frac{Z_R + jZ_{0,x}\tan(k_xW)}{1 + j\frac{Z_R}{Z_{0,x}}\tan(k_xW)}. \tag{2.22}$$

This equation is similar to the equation for translating impedance in a pipe along its length (as given, e.g., by Kinsler et al. [11]), however, the characteristic impedance used must be $Z_{0,x} = \rho_0\omega/k_x$ instead of $Z_0 = \rho_0 c$.

If the left wall is closed and rigid, the boundary condition at $x = 0$ must be replaced by $u(0,t) = 0$. Hence:

$$\begin{aligned} u(0,t) = k_x(Ae^{jk_xW} - Be^{-jk_xW}) = 0 \implies A = Be^{-2jk_xW}. \\ \text{Hence, } Z_R = Z_{0,x}\cdot\frac{\cancel{B}(e^{-2jk_xW}+1)}{\cancel{B}(e^{-2jk_xW}-1)} = Z_{0,x}\cdot\frac{e^{-jk_xW}+e^{jk_xW}}{e^{-jk_xW}-e^{jk_xW}} = Z_{0,x}\cot(k_xW) \\ \implies k_x = \frac{1}{W}\cdot\left[\arctan\left(j\frac{Z_{0,x}}{Z_R}\right) + n\pi\right], \quad n = 0,1,2,\ldots \end{aligned} \tag{2.23}$$

This equation for k_x is similar to the case of the closed waveguide, but it contains an additional term due to the influence of the slit. This additional arc-tangent term allows for a non-zero value of k_x for the case when $n = 0$ and hence this would allow leaky wave radiation for the (0,0) mode. Furthermore, since $Z_{0,x}$ depends on the wavenumber k_x, this equation cannot be solved analytically and instead, numerical methods must be used.

Expressions for the real and imaginary parts of k_x can be obtained by expressing the result in terms of the reflection coefficient, ρ_{ro}, of the radiating orifice:

$$\rho_{\text{ro}} = |\rho_{\text{ro}}|\, e^{j\phi_{\text{ro}}} = \frac{Z_i - Z_{0,x}}{Z_i + Z_{0,x}} \tag{2.24}$$

where ϕ_{ro} is the phase of ρ_{ro}.

Starting from the definition of the arc-tangent [18], we get the following:

$$\begin{aligned} k_x &= \frac{1}{W} \cdot \left[\frac{j}{2} \ln \left(\frac{j + j\frac{Z_{0,x}}{Z_i}}{j - j\frac{Z_{0,x}}{Z_i}} \right) + n\pi \right] = \frac{1}{W} \cdot \left[\frac{j}{2} \ln \left(\frac{Z_i + Z_{0,x}}{Z_i - Z_{0,x}} \right) + n\pi \right] \\ &= \frac{1}{W} \cdot \left[\frac{j}{2} \ln \left(\frac{1}{\rho_{\text{ro}}} \right) + n\pi \right] = \frac{1}{W} \cdot \left[\frac{j}{2} \ln \left(\frac{1}{|\rho_{\text{ro}}|} e^{-j\phi_{\text{ro}}} \right) + n\pi \right] \\ &= \frac{1}{W} \cdot \left[\frac{j}{2} \ln \left(\frac{1}{|\rho_{\text{ro}}|} \right) + \frac{\phi_{\text{ro}}}{2} + n\pi \right]. \end{aligned} \tag{2.25}$$

Therefore, separate equations can be obtained for the real and imaginary parts of k_x:

$$\text{Re}[k_x] = \frac{\phi_{\text{ro}} + 2n\pi}{2W} \quad \text{and} \quad \text{Im}[k_x] = \frac{1}{2W} \ln \left(\frac{1}{|\rho_{\text{ro}}|} \right). \tag{2.26}$$

Finally, k_z, and, therefore, α and β can be determined by substituting the complex value of k_x into the expression $k_z = \sqrt{k_0^2 - k_x^2}$.

Predicting the Mode Shape

The mode shape of the waves traveling inside the antenna can be found by substituting the expression found for A in Eq. (2.23) into Eq. (2.18). The resulting equation for the mode shape of mode (n,0) is

$$p_n(x,t) = B \left(e^{-jk_{x,n}(W+x)} + e^{-jk_{x,n}(W-x)} \right) e^{j\omega t} = A_{nm} e^{-jk_{x,n}W} \cos\left(k_{x,n}x\right) \tag{2.27}$$

where $k_{x,n}$ denotes k_x evaluated for mode (n,0) and A_{nm} is the amplitude of mode (n,m). The mode shape for the modes in the y-direction are the same as for a closed waveguide, since the walls are rigid on both ends in this direction. The total pressure is given by the sum of all the modes excited in the waveguide, that is

$$p(x,y) = \sum_{n,m} A_{nm} e^{-jk_{x,n}W} \cos\left(\frac{1}{W} \arctan\left(j\frac{Z_{0,x}}{Z_R} \right) + \frac{n\pi}{W}x \right) \cos\left(\frac{m\pi}{H}y \right). \tag{2.28}$$

2.3.2 Calculating the Slit Impedance

The surface impedance of a long slit can be expressed as [19, 20]

$$Z_{\mathrm{S}} = j\omega W_{\mathrm{S}} \rho_e \qquad \rho_e = \rho_0 \left[1 - \frac{\tan\left(\frac{k' H_{\mathrm{S}}}{2}\right)}{\frac{k' H_{\mathrm{S}}}{2}} \right]^{-1} \tag{2.29}$$

where W_{S} is the width of the slit as shown in Figure 2.2 and $k' = \sqrt{\frac{\omega \rho_0}{j\mu}}$, where ρ_0 is the density of air and μ is the coefficient of viscosity of air, which provides friction losses.

The general form of the radiation impedance of a long narrow slit excited by a plane wave with angle Θ from the normal and an azimuthal angle of $\Phi = 0$ to the slit axis can be formulated as [21]:

$$\frac{Z_r}{Z_0} = k_0 H_{\mathrm{S}} \left\{ \mathrm{H}_0^{(2)}(kH_{\mathrm{S}}) - \frac{\mathrm{H}_1^{(2)}(kH_{\mathrm{S}})}{kH_{\mathrm{S}}} + \frac{2j}{\pi \left(kH_{\mathrm{S}}\right)^2} + \frac{\pi}{2} \left[\mathrm{H}_1^{(2)}(kH_{\mathrm{S}}) \cdot \mathrm{S}_0(kH_{\mathrm{S}}) - \mathrm{H}_0^{(2)}(kH_{\mathrm{S}}) \cdot \mathrm{S}_1(kH_{\mathrm{S}}) \right] \right\}. \tag{2.30}$$

where $\mathrm{H}_n^{(2)}(z)$ is the Hankel function of the second kind, $\mathrm{S}_n(z)$ is the Struve function, $k = k_0 \left(1 - \sin^2 \Theta\right)$ and $Z_0 = p_0 c_0$ is the characteristic impedance of a plane wave in free air.

The complex impedance can be decomposed in terms of its real and imaginary parts as $Z_r = Z_r' + jZ_r''$. The real part of this equation can be approximated for a small value of kH_{S} as [21]:

$$\frac{Z_r'}{Z_0} = k_0 H_{\mathrm{S}} \left[\left(1 - \frac{\left(kH_{\mathrm{S}}\right)^2}{6} + \frac{\left(kH_{\mathrm{S}}\right)^4}{64} \right) \left(1 - \frac{\left(kH_{\mathrm{S}}\right)^2}{3} + \frac{\left(kH_{\mathrm{S}}\right)^4}{45} \right) - \tag{2.31}$$

$$\left(\frac{1}{2} - \frac{\left(kH_{\mathrm{S}}\right)^2}{16} + \frac{\left(kH_{\mathrm{S}}\right)^4}{192} \right) \left(1 - \left(kH_{\mathrm{S}}\right)^2 + \frac{\left(kH_{\mathrm{S}}\right)^4}{9} \right) \Bigg]. \tag{2.32}$$

This expression can be simplified further for values of $kH_{\mathrm{S}} \ll 1$ to the expression derived by Lord Rayleigh in 1904 as [22]:

$$\frac{Z_r'}{Z_0} = \frac{k_0 H_{\mathrm{S}}}{2}. \tag{2.33}$$

The imaginary part of the radiation impedance is related to the mass of air which oscillates along with the mass inside the slit. Hence, Z_r'' can be expressed in terms of an end correction, Δd, representing the length of the prism containing this oscillating mass as [21]:

$$Z_r'' = \omega \rho_0 \Delta d. \tag{2.34}$$

For a rectangular slit in a baffle wall, the end correction can be approximated by [21, 23]

$$\Delta d = -\frac{H_{\mathrm{S}}}{\pi} \ln \left[\sin\left(\frac{\pi}{2} \epsilon \right) \right] \tag{2.35}$$

where $\epsilon = \frac{H_S}{H}$ is the perforation ratio. Since the slit has two openings (inside and outside), the end correction must be multiplied by two to account for the mass oscillating on both sides of the slit.

To obtain the specific impedance of the slit the impedances must be normalised by the perforation ratio, ϵ [19].Therefore the total normalised input slit impedance can be expressed as the sum of the surface impedance, Z_S, and the radiation impedance, Z_r, as

$$Z_i = \frac{1}{\epsilon}\left(Z_\mathrm{S} + Z_r\right) = \frac{1}{\epsilon}\left(j\omega W_\mathrm{S}\rho_e + \frac{Z_0 k_0 H_\mathrm{S}}{2} + j\omega\rho_0 2\Delta d\right). \tag{2.36}$$

2.3.3 Calculating the Impedance of Periodically Spaced Holes

The surface impedance of a circular hole is given by [20]

$$Z_S = j\omega\rho_e l \qquad \rho_e = \rho_0\left[1 - \frac{2}{s\sqrt{-j}}\frac{J_1(s\sqrt{-j})}{J_0(s\sqrt{-j})}\right]^{-1} \tag{2.37}$$

where $s = r\sqrt{\frac{\omega\rho_0}{\mu}}$ and l is the length of the cylindrical hole.

The radiation impedance of a circular hole at the end of a long tube for values of $kr < 0.5$ can be approximated as [24]:

$$Z_{11} = \frac{1}{4}\rho_0 c k_0^2 r^2 + 0.6134 j\rho_0 c_0 kr. \tag{2.38}$$

The impedance at the end of a tube was chosen since for low frequencies, the baffle formed by the antenna is small compared to the wavelength and behaves similarly to a long tube [24]. Furthermore, to account for both ends of the hole, the imaginary part of Z_{11} must be multiplied by two [25].

To obtain the specific impedance of the linear array of circular holes, the impedance must be normalized by the porosity, ϕ [25]. This can be calculated as the ratio of the area of a single hole and the closed area of the surface corresponding to that hole, that is

$$\phi = \frac{\pi r^2}{bH} \tag{2.39}$$

where b is the hole separation and H is the height of the ALWA cavity as shown in Figure 2.3.

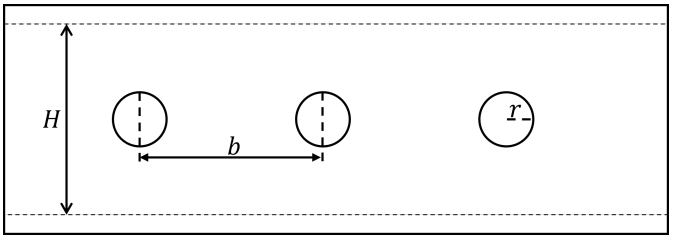

Figure 2.3: Section of the ALWA surface containing the circular holes.

Furthermore, the mutual impedance of adjacent holes needs to be considered. The mutual impedance of two identical holes with the same phase and amplitude is given by [26]

$$Z_{12} = R_{11}\left[\frac{\sin kb}{kb} + j\frac{\cos kb}{kb}\right] \tag{2.40}$$

where R_{11} is the real part of the radiation impedance of a single hole and k is the wavenumber. Considering a single hole with N holes on either side with a hole spacing of b, the total impedance of this hole would be:

$$Z_r = Z_{11} + 2 \cdot \sum_{n=1}^{N} R_{11}\left[\frac{\sin nkb}{nkb} + j\frac{\cos nkb}{nkb}\right]. \tag{2.41}$$

Since this equation is only valid if the radiators all have the same phase and amplitude, we will consider only the influence of the closest 2 holes. Hence, the total impedance of each hole becomes:

$$\begin{aligned} Z_i = \frac{j\omega\rho_0 l}{\phi}\left[1 - \frac{2}{s\sqrt{-j}}\frac{J_1(s\sqrt{-j})}{J_0(s\sqrt{-j})}\right]^{-1} \\ + \frac{\rho_0 c\left(k_0 r\right)^2}{4\phi}\left[1 + 2 \cdot \sum_{n=1}^{2}\left(\frac{\sin nkb}{nkb} + j\frac{\cos nkb}{nkb}\right)\right] + 2 \times 0.6134 j\frac{\rho_0 c}{\phi}kr. \end{aligned} \tag{2.42}$$

2.4 Metamaterial ALWAs

The negative refractive index, made possible by the use of metamaterials, allows the ALWA to radiate not only in the endfire quadrant, but also in the backfire quadrant. In 2010, Bongard et al. [5] proposed a design for a Transmission Line (TL) metamaterial with negative, zero and positive refractive indices. This metamaterial was used to design an ALWA and tested experimentally by Naify et al. in 2013 [6].

2.4.1 Using Electroacoustic Analogies for Modeling ALWAs

Acoustic components can be modeled with analogies to the three main lumped elements of electromagnetic elements. Acoustic masses can be modeled as an inductance and an acoustic compliance is analogous to a capacitance. Losses and radiation can be modeled using a resistance element. [27]

The components of a metamaterial ALWA can be modeled using combinations of these elements. A section of waveguide can be modeled as a series mass with a parallel compliance. An open duct that is short compared to the wavelength can be modeled as a shunt mass and resistance. Finally, a membrane that is clamped at the edges is modeled as a mass or compliance, for lower or higher frequencies respectively [27].

2.4.2 Obtaining Negative Refractive Index

A natural material with a positive refractive index can be modeled in TL theory as a mass element in series with a compliance element in parallel. The dual topology of this set-up,

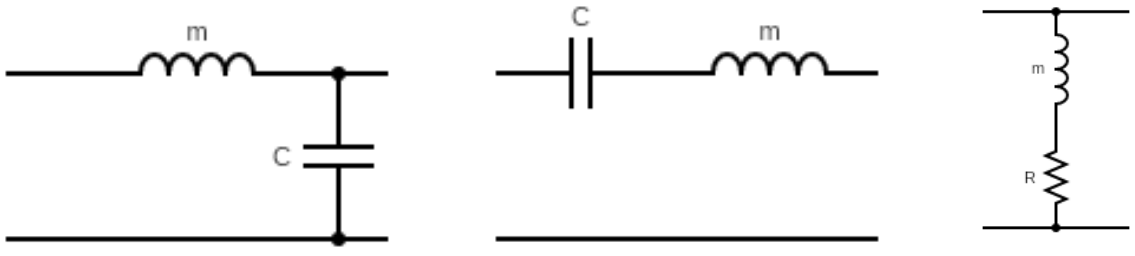

(a) Waveguide Section. **(b)** Membrane. **(c)** Short Open Duct.

Figure 2.4: Equivalent circuits of the different metamaterial ALWA components.

that is, a compliance element in series with a mass element in parallel produces a negative refractive index. It should be noted that the dual topology can only be achieved by using a periodic loading of shunt masses and series compliances. By combining the elements of the natural material and the dual topology into a single unit cell, a Composite Right/Left Hand (CRLH) TL can be achieved, that is a material which can have either positive or negative refractive indices depending on the frequency. At low frequencies, the elements of the dual topology dominate and produce a negative refractive index (Left Hand band), while at higher frequencies, the natural material elements dominate, resulting in a positive refractive index (Right Hand band). Using this design, it is possible to achieve a smooth transition between the left and right hand bands. [5]

The physical design suggested by Bongard et al. [5] and tested by Naify et al. [6] consisted of a cylindical waveguide operating in its dominant mode region (plane waves). The unit cells of the metamaterial were composed of a membrane surrounded by narrow open channels on both sides.

2.4.3 Metamaterial ALWA Properties

The ALWA parameters for the metamaterial structure can be calculated using Bloch theory. This theory states that the propagation constant is given by [6]:

$$\gamma_B = \alpha + j\beta_B = \arccos\left(1 - \frac{X^2}{2}\right), \qquad X = \frac{\omega}{\omega_R} - \frac{\omega_L}{\omega} \tag{2.43}$$

where ω_R and ω_L are the right and left hand cut-off frequencies, respectively, defined by [6]:

$$\omega_R = \frac{1}{\sqrt{(M_{\text{shunt}} + M_{TL})\,(C_{\text{shunt}} + C_{TL})}}, \qquad \omega_L = \frac{1}{\sqrt{M_{TL} C_{\text{mem}}}}. \tag{2.44}$$

Here, the terms labeled M and C are the mass and compliance of the shunt, TL and membrane components (as indicated by the subscripts) which depend on the geometry of the ALWA unit cell [5, 6]. Below ω_L and above ω_R, no propagation can occur in the waveguide [6]. It is possible to have a band gap between the positive and negative index regions; however, by tuning the parameters of the ALWA, this gap can be closed [6].

Between $f_L = \omega_L/2\pi$ and $f_R = \omega_R/2\pi$, Bongard et al. [5] identified three key frequencies of the metamaterial structure important for ALWA applications. They used a dispersion diagram to demonstrate these frequencies and denoted them as f_0, f_1 and f_2. The dispersion diagram is a plot of the Bloch parameter, β_B multiplied by the lattice constant, d, which represents the length of a single unit cell, plotted against the frequency. The frequency f_0 is the transition frequency at which the refractive index goes from negative to positive. This frequency occurs when $\beta_B d = 0$ and for ALWA applications, this corresponds to radiation at broadside.

The frequencies f_1 and f_2 are the frequencies where the dispersion curve intersects with the light lines (the dispersion curve in free air, $k = \pm\frac{\omega}{c}$). In the range $f_1 < f < f_2$, the waves propagating within the waveguide satisfy the condition $-k_0 < \beta < k_0$, and therefore leaky wave radiation can occur in this frequency range. The frequency f_1 is associated with radiation at backfire while f_2 is associated with radiation at endfire. Outside of this range, Bongard et al. [5] predicted that there should be very little radiation.

2.5 Applications of ALWAs

2.5.1 Acoustic Dispersive Prism

In 2016, Esfahlani et al. [7] created an ALWA which could act as an acoustic prism, analogous to the optical prisms which can split light into its different frequency components. Designing such an acoustic dispersive prism is difficult compared to an optical prism due to the two requirements that need to be met. The prism must be both dispersive and have a low reflectivity. While these conditions are easily met in optics by shaped glass in air, in acoustics, dispersion is typically negligible and there is often a large difference in the impedance of a material and its surrounding medium.

Esfahlani et al. [7] noticed that with the use of a metamaterial ALWA, these problems can be overcome. The CRLH TL metamaterial provides dispersion characteristics with refractive indices ranging from negative to positive values. The impedance mismatch is overcome due to the leaky wave nature of the ALWA. The matching of the parallel components of the wavenumbers in the antenna and the surrounding medium causes waves to leak from the waveguide and radiate at different angles according to the frequency.

The design for the dispersive acoustic prism proposed by Esfahlani et al. [7] achieved results comparable to a superprism in the near-field with a compact design that is only about twice the length of the wavelength. A superprism separates the frequency components of a wave into significantly different angles. Esfahlani et al. also note that in the far-field, the same ALWA design operated in the receiving mode leads to another useful application as a direction finding device.

2.5.2 Single Microphone Direction Finding

Esfahlani et al. [8] used a metamaterial ALWA design similar to the design proposed by Bongard et al. [5] to demonstrate single microphone direction finding. The design of Esfahlani et al. differs from Bongard et al. by using flanged cylindrical ducts instead of

axisymmetric open channels. This was done to limit the radiation and sound detection to a single half-space. The ALWA was also placed in a wooden baffle for the measurements.

Esfahlani et al. [8] tested this antenna in both the radiating mode and the receiving mode with FEM simulations and experimental measurements and found good agreement between these and their theoretical model. The receiving mode uses a microphone placed inside the ALWA to detect the direction of an external sound source. The conclusion of the study was that the ALWA design possesses a monotonically increasing direction with frequency, which is suitable for single microphone direction finding in the receiving mode.

In 2016, Woolfe et al. [9] conducted a study about adapting metamaterial ALWAs for underwater applications. Due to the small difference between the impedance of the water and the walls of the waveguide, the walls of the antenna can no longer be considered rigid. This can be used as a part of the design, since the walls will radiate leaky waves without requiring holes in the ALWA. It is important to consider that in this case, the impedance of the material chosen to construct the walls will have a considerable effect on the properties of the ALWA. Woolfe et al. proposed the use of the wall thickness for tuning the radiation pattern. If the thickness is varied along the length of the antenna with a constant gradient, the radiation angle will move towards the side with the thinner wall. This is due to the lower impedance of the thin wall, and hence the greater radiation. The design proposed by Woolfe et al. is limited to radiation in the endfire quadrant, since it does not incorporate metamaterials.

2.6 Modulation of the Design Parameters for Practical Applications

Modulating the parameters of the ALWA along its length can be used for various applications. One such application is the suppression of side-lobes for improved directional radiation capabilities. In 2019, Lan et al. [28] designed a gradient amplitude ALWA consisting of 39 unit cells chosen from 9 different designs. Each unit cell was composed of a straight pipe with a clamped membrane, open channel and side-mounted Helmholtz resonator. The width of the channel was tuned to achieve the desired radiation profile, however such a modulation would introduce a phase change. To compensate for this Lan et al. used Helmholtz resonators with tuned sizes to counteract the phase shift. They verified their design using Finite Element Method (FEM) simulations, achieving successful suppression of the side-lobes while preserving the quality of the main-lobe.

In the electromagnetic domain, modulated LWAs have been successfully used for achieving novel radiation patterns. One such radiation pattern is the radiation of broad-beam patterns as presented by Gomez-Tornero et al. [29]. The design presented utilized modulation of the slot width and the slot position from the edge of the LWA to tune the scanning range and broad beam shape. Using tapering of the same parameters, Gomez-Tornero et al. [30] achieved a focusing of the radiation to a specific point in the near-field, hence acting as a Leaky Wave Lens. The focal region of the Leaky Wave Lens could be scanned

by changing the frequency.

By obtaining a TRE from the TEN for a particular type of ALWA, it becomes possible to determine the modulations required to achieve specific radiation patterns. This was demonstrated by Martinez-Ros et al. [31] for substrate integrated waveguide line-source LWAs. Martinez-Ros et al. successfully manufactured and measured LWAs with reduced side-lobes for frequency scanning, broad-beam radiation, radiation nulls and near-field focusing using the TRE presented in their work.

3

Methodology

This chapter discusses the methods employed for calculating numerical solutions of the theoretical model and the procedures employed for the verification of this model. A detailed description of the set-up of the Finite Element Method model in Comsol is provided. Finally, the construction and measurement of the physical prototypes are described and discussed.

3.1 Numerical Solution of the Theoretical Model

Since the equation for the complex propagation constant in the x-direction, k_x, cannot be solved analytically, a numerical solution is used instead. First, an estimate for the model was calculated by solving the equation

$$k_x = \frac{1}{W}\left[\arctan\left(\frac{Z_0}{Z_i}\right) + n\pi\right] \tag{3.1}$$

where $Z_0 = \rho_0 c$ was used instead of $Z_{0,x} = \rho_0\omega/k_x$ to obtain an initial estimate.

This estimate was used as the starting point for the `fminsearch` command in Matlab. This command uses the Nelder-Mead simplex algorithm to find a local minimum of the given function [32]. The Nelder-Mead simplex algorithm iteratively modifies the value of the variable until the stopping criteria are met [33].

A function was defined that would calculate the error between the estimate of the previous iteration, $k_{x,\mathrm{ini}}$, and the result of the model calculated with $Z_{0,x} = \rho_0\omega/k_{x,\mathrm{ini}}$. The impedance of the radiating orifice, Z_i, was assumed to not vary significantly with k_x. Hence, Z_i was not recalculated within the optimization algorithm. A loop was constructed to minimize the error function using the `fminsearch` command at every frequency, which yields the values of k_x that satisfy the TRE (i.e. Eq. 2.23) for all frequencies.

3.2 Simulating the ALWA in Comsol

To validate the theoretical model, simulations were carried out in Comsol Multiphysics version 6.2, a simulation software that can perform Finite Element Method (FEM) calculations.

3.2.1 Constructing the Geometry

The geometry of the ALWA was defined in Comsol by creating the shape of the air inside the antenna and in a small volume surrounding it. The solid material of the ALWA was assumed to be a perfectly rigid material. The shape of the air inside the ALWA was created using rectangles and difference functions. The region of air outside the ALWA was created by using a sphere which was truncated at the top, bottom and backside to reduce computation time. It was ensured by trial and error that not too much volume was truncated or that the sphere was not made so small that the results of the simulation would be significantly affected.

The dimensions of the ALWA model were parametrized, so that simulations can be run for different sets of parameters. The parameters used are shown in Table 3.1.

Table 3.1: Table of parameters for the ALWA model

General Dimensions	Slit Dimensions	Hole Dimensions
H - ALWA Cavity Height	H_S - Slit Height	r - Hole Radius
W - ALWA Cavity Width	O_S - Slit Offset	b - Hole Separation
L - ALWA Length		O_H - Hole Offset
d - Wall Thickness		

Two sizes of ALWA were chosen to simulate the two modes under consideration. The small antenna chosen for simulating the (0,0) mode has the dimensions

$$H = 16 \text{ mm}, \qquad W = 46 \text{ mm}, \qquad L = 1.75 \text{ m}, \qquad d = 2 \text{ mm}, \qquad O = 20 \text{ mm}$$

and the large antenna chosen for simulating the (1,0) mode has the dimensions

$$H = 35 \text{ mm}, \qquad W = 95 \text{ mm}, \qquad L = 1.5 \text{ m}, \qquad d = 2.5 \text{ mm}, \qquad O = 20 \text{ mm}.$$

These dimensions were chosen since they would result in a cut-off frequency that is low enough for reasonably fast computation time. Another consideration was that material was available for purchase in these dimensions for experimental verification. The length of the antenna, L, was chosen such that it is around five times the wavelength corresponding to the cut-off frequency in free air. The slit/hole offset, O, defines the distance between the source and the start of the slit/holes. This was chosen to be small enough that there are no resonances that can occur along this length below the cut-off of the (0,0) mode.

3.2.2 Setting the Boundary Conditions

The external boundaries of the truncated sphere were set with the Perfectly Matched Boundary (PMB) condition. This condition applies the classical Perfectly Matched Layer (PML) to a surface, which prevents strong reflections from occurring at this boundary [34]. These external surfaces were also set with the External Field Calculation setting, which allows for the extrapolation of the sound field outside the boundaries of the model [35]. This was used to calculate the directivity of the ALWA in the far-field, at a distance of 10 m. The walls of the ALWA, except the source and termination walls, were

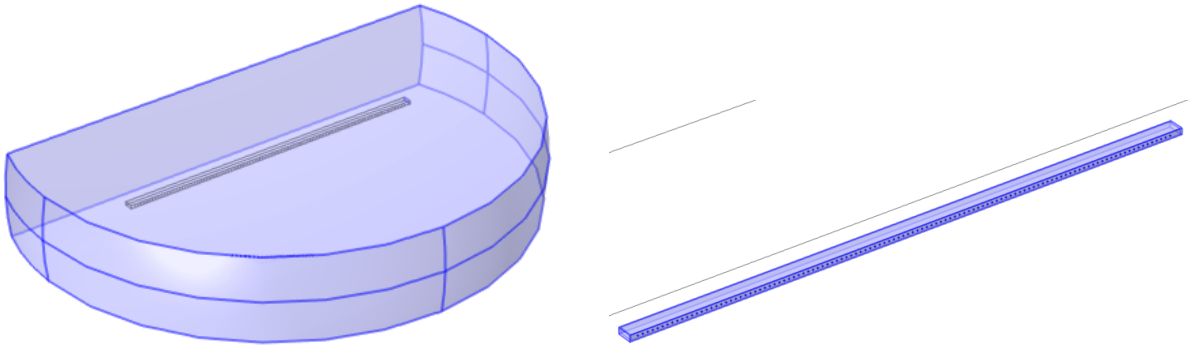

(a) Perfectly Matched Boundary. **(b)** Sound Hard Boundary.

Figure 3.1: Boundary condition imposed on the different surfaces.

modeled as solid reflective boundaries. This imposes the rigid wall condition on these surfaces [36].

In the ideal case, there should not be any reflections at the termination wall. This was modeled in Comsol using a PMB at the wall of the termination. In practice, the termination may be created by putting mineral wool in the end of the antenna to absorb most of the sound energy.

Simulating the (0,0) Mode

For exciting the (0,0) mode in the ALWA, a velocity source condition was imposed on the source wall such that this has a velocity of 0.1 m s^{-1}. In practice, this is equivalent to using a single loudspeaker or two loudspeakers operating in phase with each other.

Simulating the (1,0) Mode

Using a monopole source like for simulating the (0,0) mode in the frequency range of the (1,0) mode results in the formation of two lobes simultaneously. Hence, to excite the (1,0) mode in the ALWA to a larger extent than the (0,0) mode, the source wall was split into two halves. One half was set with a velocity of 0.1 m s^{-1} and the other half was set with a velocity of -0.1 m s^{-1}. In practice, this is equivalent to using two loudspeakers operating with a 180° phase difference.

3.2.3 Setting the Mesh Size

The mesh size should ideally be about 1/6 of a wavelength [37]. If a constant mesh size were used, corresponding to the mesh size needed for the highest frequency, the computation time would be very long. Therefore, the mesh size was set to vary in size with the frequency so that the simulations at lower frequencies are faster. In practice, a mesh size of 1/5 of the frequency was found to be sufficient to obtain satisfactory results that matched theoretical predictions, allowing shorter computation times. The mesh was constructed from free tetrahedral quadratic Lagrange elements.

3.2.4 Determining the Design Parameters from the Simulations

Post-processing was required to determine the design parameters from the results of the simulations, which can be compared to the predictions of the theory model.

Angle of Radiation

A directivity plot was generated in Comsol from the External Field Calculation sound pressure level data and exported as a text file. This file was loaded into Matlab and the `max` command was used to find the angle corresponding to the maximum value of the sound pressure level. This maximum would correspond to the position of the main lobe of the radiation pattern. The input of the `max` command was restricted so that only data between 0° and 90° were used to avoid capturing the lobe on the back of the antenna.

Leakage Rate

The leakage rate was estimated by calculating a surface integral of the active intensity on a plane inside the cavity of the ALWA at a position close to the source and a position close to the termination. This integration gives the power flowing through that surface. The distance between the two planes was noted and the value of the leakage rate was then calculated using Eq. (2.9).

3.3 Measuring Two Prototype ALWA Designs

3.3.1 Manufacturing the ALWAs

The ALWA was manufactured from rectangular aluminum tubes. Due to limitations on the procurement of the necessary materials, only ALWA designs with circular holes were tested. Two sets of dimensions were chosen for the experimental measurements. A small antenna was constructed from a tube with inner dimensions of 16 mm × 46 mm and a wall thickness of 2 mm. This antenna was cut to a length of 1.75 m. Holes were cut on one face of the tube with a radius of $r = 2$ mm and a center-to-center hole separation of $b = 15$ mm. The dimensions of this antenna were chosen such that the cut-off frequency of the (0,0) mode would lie around 1 kHz.

The holes of the small antenna were cut using a water pressure cutter as shown in Figure 3.2a. This cutting method was chosen since it is fast and precise. Also, this method leaves less burrs on the inside of the ALWA compared with drilling, which would be difficult to remove due to the length of the tube. The bed of the water pressure cutter was smaller than the length of the ALWA, whereby it was cut into two smaller pieces that were treated separately. The two pieces were aligned using an aluminum support and metal wires and the gap was sealed with tape.

A large antenna was constructed from a tube with inner dimensions of 35 mm × 95 mm and a wall thickness of 2.5 mm. The large antenna was cut to a length of 1.5 m. Holes were cut on one face of the tube with a radius of $r = 4$ mm and a center-to-center hole separation of $b = 30$ mm. The dimensions of this antenna were chosen such that the cut-off frequency of the (1,0) mode would lie around 2 kHz.

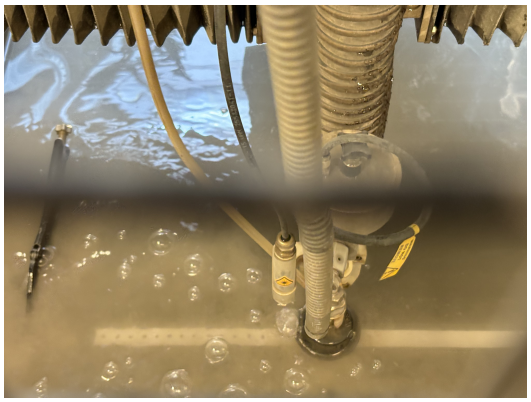

(a) Water Cutting.

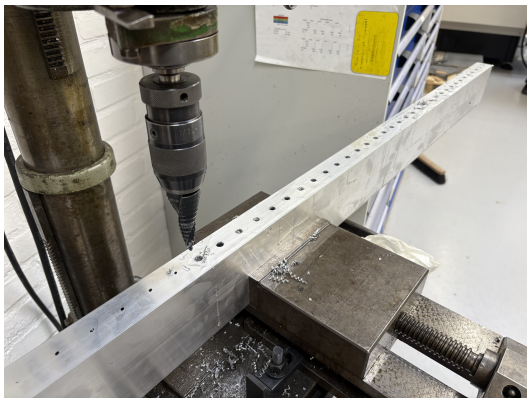

(b) Drilling.

Figure 3.2: Cutting techniques for making the holes in the aluminum tube.

The holes of the large antenna were drilled using a milling machine as shown in Figure 3.2b. This method was chosen since the smaller number of holes meant that drilling would be more efficient for manufacturing than by using the water cutter. The larger size of the holes also allowed for the holes to be deburred from the outside.

A sound source is needed for the ALWA to operate in the radiating mode. Plastic fixtures were manufactured using 3D-printing to hold the loudspeakers in place at the source end. The fixtures were attached to the ALWAs and sealed using tape. Two different terminations were made to test different conditions. An absorbing termination was made by folding a sample of mineral wool and placing this inside the end of the ALWA. A reflecting termination was made by cutting a plate of aluminum that was attached using tape to cover the end of the ALWA. The ALWA prototypes, loudspeaker fittings and terminations are shown in Figure 3.3.

(a) ALWAs.

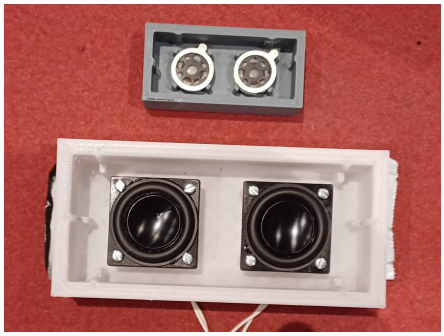

(b) Loudspeaker Fittings.

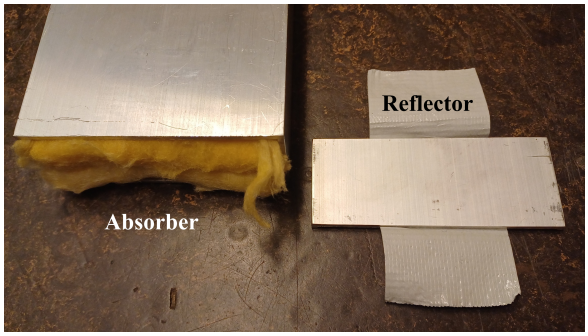

(c) Terminations.

Figure 3.3: The manufactured ALWAs, loudspeaker fittings and terminations.

3.3.2 Apparatus and Set-up

Audio Interface

A Focusrite Scarlett 4i4 Audio Interface, shown in Figure 3.4, was used to connect the audio devices to the measurement computer. The audio interface was connected to the computer using a USB connector. The computer supplied the output signal for the loudspeakers and received the measurement data from the microphone. The input channel of the audio interface was connected to the microphones (via the power module), and the output channel was connected to the loudspeakers (via the power amplifier). A loop-back was connected from one of the output channels to an input channel to directly measure the loudspeaker's input signal.

(a) Front Panel. **(b)** Back Panel.

Figure 3.4: The Focusrite 4i4 Audio Interface.

Power Module and Measurement Microphone

A GRAS Power Module Type 12AA (Figure 3.5a) was used to supply the GRAS 46AF free-field measurment microphone (Figure 3.5b) with the required voltage. The input channel was connected to the microphone, while the output channel was connected to the Audio Interface. A free-field microphone was chosen, since the anechoic chamber is designed to simulate free-field conditions. A second microphone of the same model was used for repeated readings.

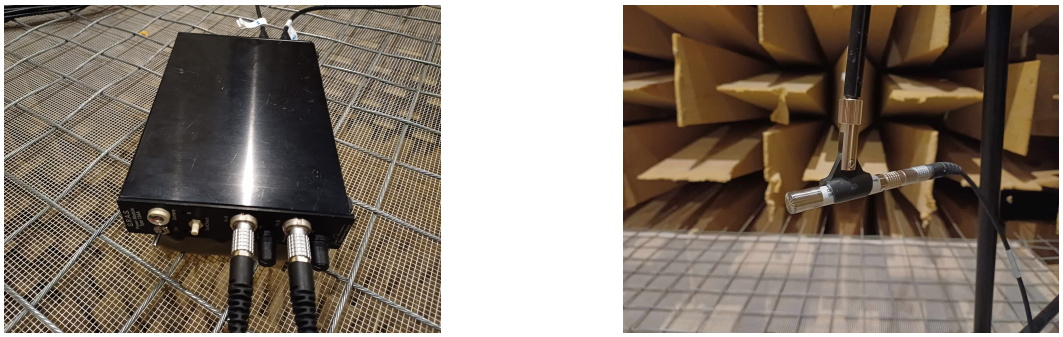

(a) Microphone Power Module. **(b)** Microphone.

Figure 3.5: The GRAS Power Module Type 12AA and GRAS 46AF Free-Field measurement microphone.

Power Amplifier

A Fosi Audio ZA3 Power Amplifier, shown in Figure 3.6 was used to amplify and supply the signal for the loudspeakers. The output was set in Mono mode, since only one loudspeaker signal was needed. The output channels were connected to a phase switch inside the anechoic chamber. The input signal was supplied from the Audio Interface.

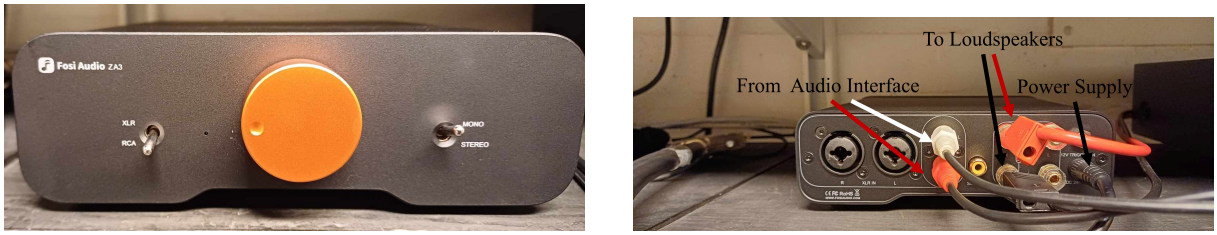

(a) Front Panel. **(b)** Back Panel.

Figure 3.6: The Fosi Audio ZA3 Power Amplifier.

Phase Switch

The phase switch is a in-house built switch which takes a single input signal and provides two output signals for powering two loudspeakers. The switch has two settings. In the 0° setting, the two loudspeakers are fed with the same signal in phase. In the 180° setting, one of the loudspeakers is fed with the original input signal while a phase difference of 180° is applied to the other. The phase switch is shown in Figure 3.7.

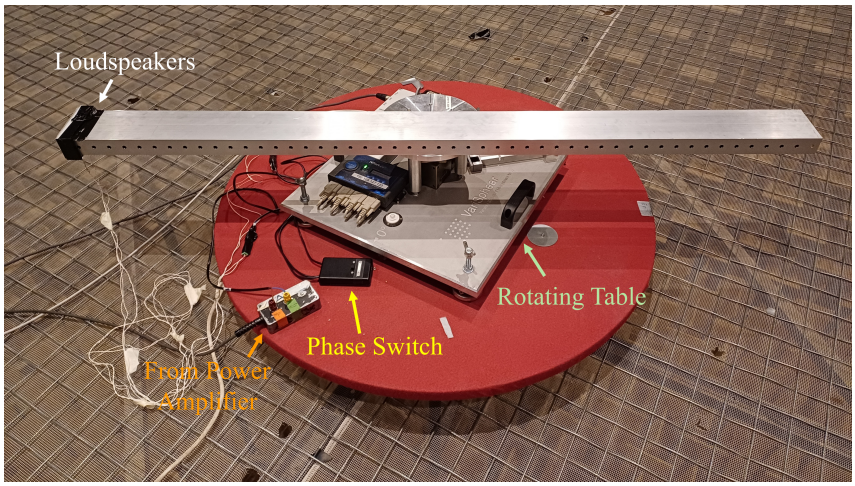

Figure 3.7: The ALWA placed on the rotating table with the loudspeakers attached and connected to the phase switch.

Rotating Table

A Varisphear rotating table, shown in Figure 3.7, was used to rotate the ALWA so that the frequency response function could be measured at different angles. The rotating table was controlled by the measurement computer via a network cable. The rotating table was powered by a Power Supply Unit placed outside the anechoic chamber.

Loudspeakers

Two different models of loudspeakers were used for the two sizes of antennas. For the small antenna, a pair of Visaton K-16 loudspeakers were used. These loudspeakers have a diameter of 16 mm and fit inside the cross-section of the small antenna. For the large antenna, a pair of Visaton BF 32 S WP loudspeakers were used. These loudspeakers have a flange with dimensions 32×32 mm and fit within the large antenna. The loudspeakers were attached to each respective fitting as shown in Figure 3.3b, and the fitting was attached to the ALWA and secured with tape. The loudspeakers were connected to the two outputs of the phase switch, allowing these to be operated in or out of phase.

3.3.3 Measurement Procedure

After all the equipment was set up and connected as described above, the ALWA was mounted on the rotating table using double-sided tape. The initial angle, θ_i, was measured before starting the directivity measurements. This was done by measuring the perpendicular distances x_m and y_m as shown in Figure 3.8a from the microphone to the center of the ALWA. The initial angle can then be determined as:

$$\theta_i = \arctan \frac{y_m}{x_m}. \tag{3.2}$$

The uncertainty of the measurement of the perpendicular distances was estimated to be ± 10 cm due to the movement of the net while standing at different positions. The uncertainty of the initial angle can be calculated as [38]

$$\Delta\theta_i = \sqrt{\left(\frac{\partial\theta_i}{\partial x_m}\Delta x_m\right)^2 + \left(\frac{\partial\theta_i}{\partial y_m}\Delta y_m\right)^2} = \sqrt{\left(\frac{y_m \Delta x_m}{x_m^2 + y_m^2}\right)^2 + \left(\frac{x_m \Delta y_m}{x_m^2 + y_m^2}\right)^2} \tag{3.3}$$

where Δx_m and Δy_m are the uncertainty of x_m and y_m respectively.

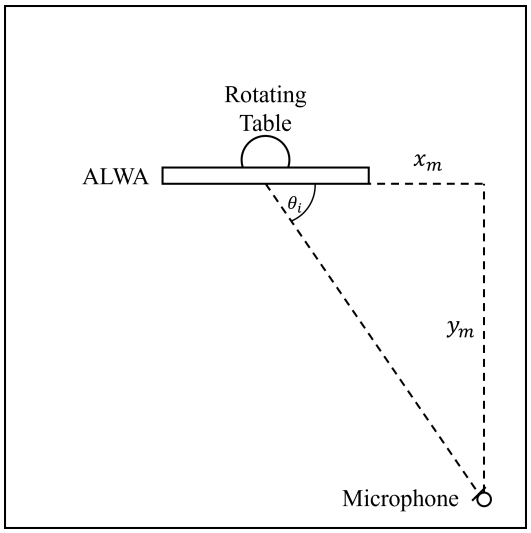

(a) Geometry of the set-up.

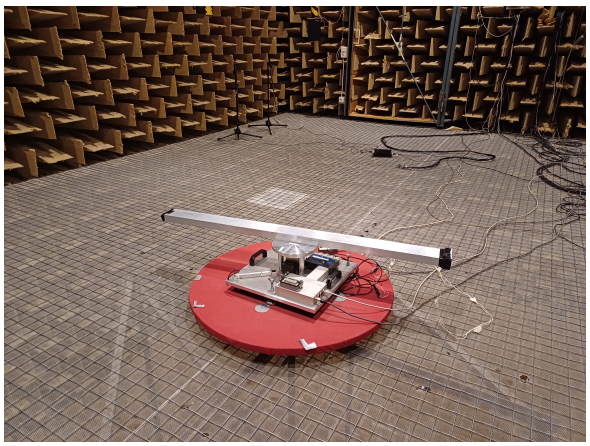

(b) Photo of the Set-up.

Figure 3.8: The measurement set-up.

A Matlab program was used to generate sine sweep signals and perform linear deconvolution to obtain the frequency response function of the system. This method can be performed efficiently by padding the signal with zeros to double the Fast Fourier Transform (FFR) block length and then applying the FFT to both the input and output signals. The output spectrum is divided by the input spectrum and the impulse response can be obtained using an inverse FFT [39].

The Matlab program was configured to rotate the ALWA in intervals of 1° and perform the sweep measurement at each angle, saving each of the resulting impulse response functions. An FFT was performed on the measured impulse response for each measured angle to obtain the directivity of the antenna, which is the magnitude of the frequency response function.

The measurement was repeated for different microphone positions, measuring up to two positions simultaneously. The two ALWAs were measured in four different microphone positions for all possible combinations of termination (absorber or reflector) and source (monopole or dipole). The measurements taken are summarized in Table 3.2.

Table 3.2: Summary of measurements.

ALWA	Termination	Source	Positions
Large	Absorber	Monopole	1-4
		Dipole	
	Reflector	Monopole	
		Dipole	
Small	Absorber	Monopole	5-8
		Dipole	
	Reflector	Monopole	
		Dipole	

The microphone positions were recorded and are listed in Table 3.3.

Table 3.3: Microphone Positions.

Position	x_m / cm	y_m / cm	θ_i
1	240 ± 10	450 ± 10	$62° \pm 1°$
2	210 ± 10	210 ± 10	$45° \pm 2°$
3	240 ± 10	260 ± 10	$47° \pm 2°$
4	230 ± 10	360 ± 10	$57° \pm 1°$
5	250 ± 10	450 ± 10	$61° \pm 1°$
6	250 ± 10	230 ± 10	$43° \pm 2°$
7	240 ± 10	370 ± 10	$57° \pm 1°$
8	240 ± 10	300 ± 10	$51° \pm 1°$

The measured directivities were used to determine the radiation angle by finding the angle of the maximum magnitude. This was made using the `max` command in Matlab in the same way as for the Comsol simulation results. The directivity was then normalized with respect to the maximum value for each frequency and converted to a decibel scale.

The leakage rate was estimated from the magnitude of the reflected lobe in the backfire quadrant, using the measurements terminated with the reflector, as [40]

$$\frac{\alpha}{k_0} = \frac{G_{fwd}(dB) - G_{bwd}(dB)}{k_0 \cdot 20L\log_{10}(e)} \tag{3.4}$$

where $G_{fwd}(dB)$ and $G_{bwd}(dB)$ are the gains of the forward and backward lobes in dB, respectively, and L is the length of the antenna.

The radiation angle and leakage rate obtained from each microphone position were averaged. The uncertainty of the averaged values was calculated using the following formula [41]

$$\text{Uncertainty} = t_{0.025,n-1} \times \frac{s}{\sqrt{n}} \tag{3.5}$$

where s is the standard deviation, n is the number of measurements and $t_{0.025,3} = 3.18$ is determined form Student's t distribution such that the uncertainty represents a 95 % confidence interval.

4

Results and Discussion

This chapter presents the results of the theoretical model, the FEM simulations and the experimental measurements. Plots of the radiation angle and leakage factor are shown for different dimensions of the ALWA. Directivity plots, sound pressure plots and sound pressure level plots are also shown for the FEM simulation. Finally, the experimental measurements, the Comsol simulations and the theoretical model are compared for the ALWA with holes in two different sizes.

4.1 Predicted Properties of the ALWA

The theory predicts that the antenna should produce radiation for different modes (n,0) in the x-direction. Each mode has a cut-off frequency, below which the ALWA radiates at a constant angle close to broadside. Above the cut-off, the radiation angle increases with frequency non-linearly as shown in Figure 4.1a. When the ALWA is excited by a source that has equal velocity along the cross-section of the cavity, all modes that have a cut-off frequency lower than the excitation frequency are excited simultaneously. In Figure 4.1a, the (0,0) and (1,0) modes are plotted.

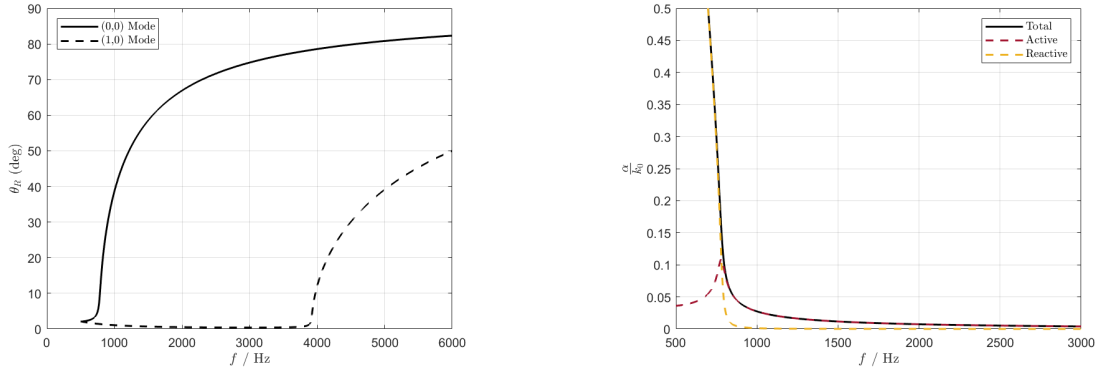

(a) Radiation Angle. **(b)** Leakage Factor.

Figure 4.1: Trends of the Radiation Angle and leakage factor predicted by the theory.

The total normalized leakage factor and its active and reactive components are shown in Figure 4.1b. The total leakage factor below the cut-off is high and decreases as it approaches the cut-off frequency. The reactive component of α dominates in this frequency

range. Above the cut-off frequency, the total leakage factor decreases. At frequencies significantly above the cut-off, the change of the leakage factor with frequency is very small. Above the cut-off frequency, the active component of α dominates. At the cut-off frequency, the active and reactive components of α are of equal size.

4.2 Plots of the Comsol simulation results

From the Comsol simulation, directivity plots and surface plots are made of the pressure and sound pressure level (SPL) on the plane parallel to the length of the antenna intersecting through the midpoint of the antenna along its height.

4.2.1 Directivity Plots

The directivity plots shown in this section were exported from Comsol, normalized with respect to the maximum SPL and truncated to show only data which is within 20 dB of the maximum. The plots on the left side in this section depict the directivity for frequencies below the cut-off frequency of the mode $(n,0)$, $f_{c,n}$, and the simulated frequency that is closest to the cut-off. The figures on the right show the directivity for the frequencies above the cut-off frequency.

(0,0) Mode

The directivity plots for the small antenna with a slit with $H_s = 3$ mm and with holes with $r = 2$ mm and $b = 15$ mm, operated in the (0,0) mode with a monopole source, are shown in Figures 4.2 and 4.3 respectively. The cut-off frequency of the (0,0) mode predicted by the theoretical model is $f_{c,0} \approx 1230$ Hz for the slit ALWA and $f_{c,0} \approx 780$ Hz for the ALWA with holes.

For frequencies significantly below $f_{c,0}$, the directivity is almost omnidirectional. As the frequency approaches $f_{c,0}$, the directivity becomes more elliptical with the major axis pointing at 0°. Above $f_{c,0}$, lobes start to appear whose angle increases with increasing frequency. For frequencies just above the cut-off, the beam-width is larger.

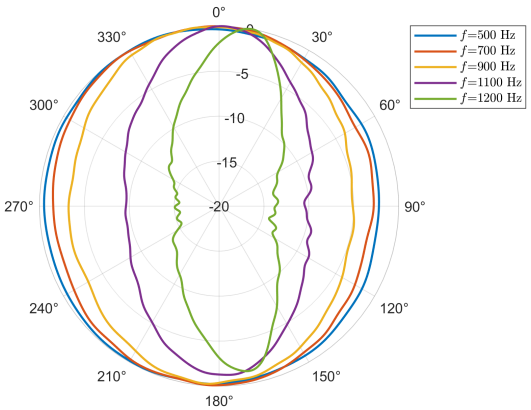

(a) Slit ALWA, $f \lessapprox f_{c,0}$.

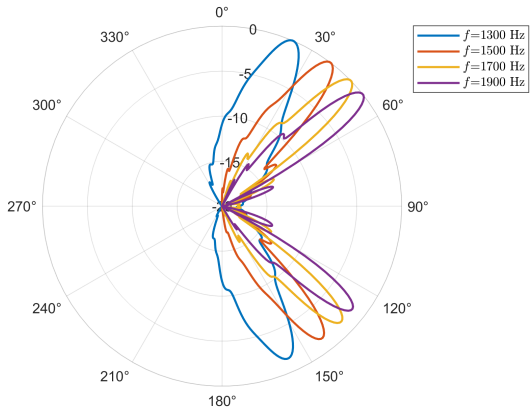

(b) Slit ALWA, $f > f_{c,0}$.

Figure 4.2: Directivity plots of the slit ALWA operated in the (0,0) mode.

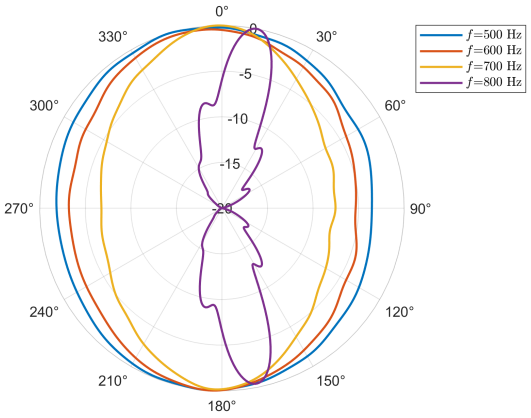

(a) Holes ALWA, $f \lessapprox f_{c,0}$.

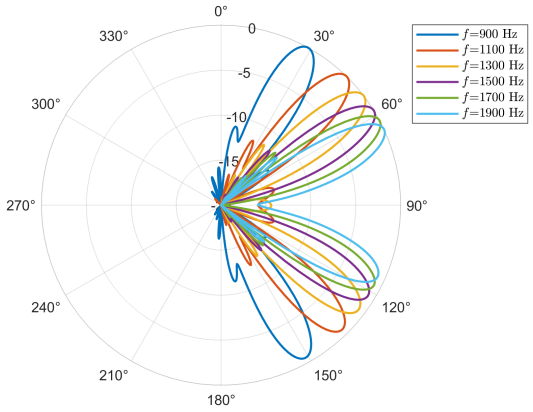

(b) Holes ALWA, $f > f_{c,0}$.

Figure 4.3: Directivity plots of the ALWA with circular holes operated in the (0,0) mode.

(1,0) Mode

The directivity plots for the large antenna with a slit with $H_s = 3$ mm and with holes with $r = 4$ mm and $b = 30$ mm, operated in the (1,0) mode with a dipole source are shown in Figures 4.4 and 4.5 respectively. The cut-off frequency of the (1,0) mode predicted by the theoretical model is $f_{c,1} \approx 2000$ Hz for the slit ALWA and $f_{c,1} \approx 1910$ Hz for the ALWA with holes.

Below $f_{c,1}$, the directivity is partly elliptical with the major axis pointing toward 0°. However, a small lobe can be detected near endfire which corresponds to the radiation angle of the (0,0) mode. The magnitude of this lobe becomes smaller relative to the maximum as the frequency approaches $f_{c,1}$ and the (1,0) mode becomes dominant. Hence, it can be concluded that the dipole source successfully isolates the (1,0) mode from the (0,0) mode. Above $f_{c,1}$, distinct main lobes appear whose angle increases with increasing frequency. The beam-width of the lobes in this mode is narrower than for the (0,0) mode for both the case of the slit and the circular holes.

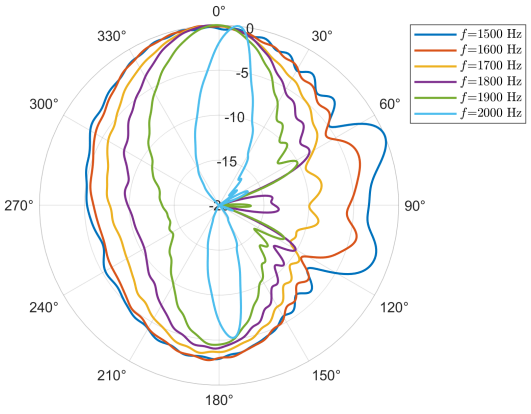

(a) Slit ALWA, $f \lessapprox f_{c,1}$.

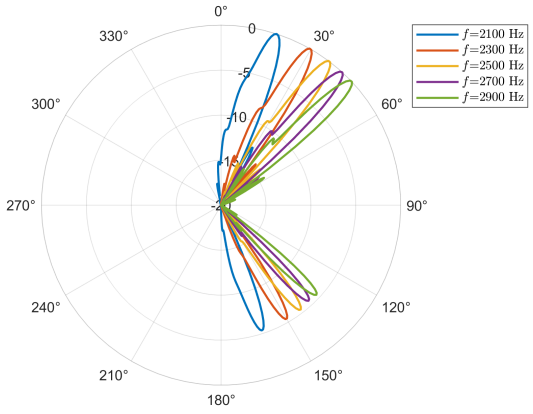

(b) Slit ALWA, $f > f_{c,1}$.

Figure 4.4: Directivity plots of the ALWA operated in the (1,0) mode from Comsol

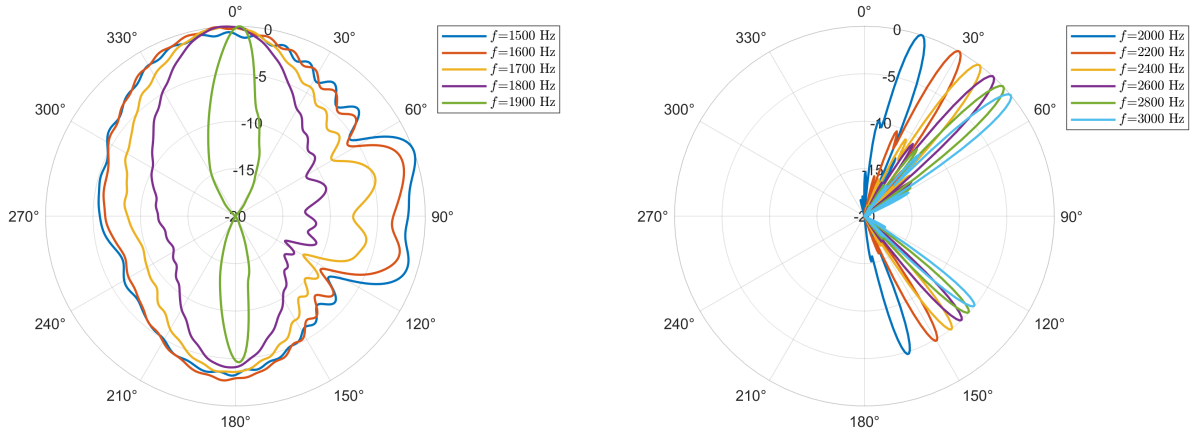

(a) Holes ALWA, $f \lessapprox f_{c,1}$.

(b) Holes ALWA, $f > f_{c,1}$.

Figure 4.5: Directivity plots of the ALWA operated in the (1,0) mode from Comsol.

4.2.2 Pressure Plots

Pressure plots for the small antenna with circular holes with $r = 2$ mm and $b = 15$ mm, operated with a monopole source, are shown for different frequencies in Figure 4.6. The cut-off frequency for this antenna in the (0,0) mode is about 780 Hz. Hence, Figure 4.6a shows the behavior of the antenna below the cut-off frequency of the (0,0) mode. It can be seen that the sound pressure inside the ALWA decays quickly along the length of the antenna. The radiation pattern is similar to a point source at this frequency.

Figures 4.6b and 4.6c show the pressure field of the ALWA when it is operated above the cut-off of the (0,0) mode. A wave can be clearly observed to propagate inside the ALWA with a decreasing wavelength as the frequency increases. The radiation shown is clearly directional, forming a series of wavefronts with a consistent angle that increases with frequency.

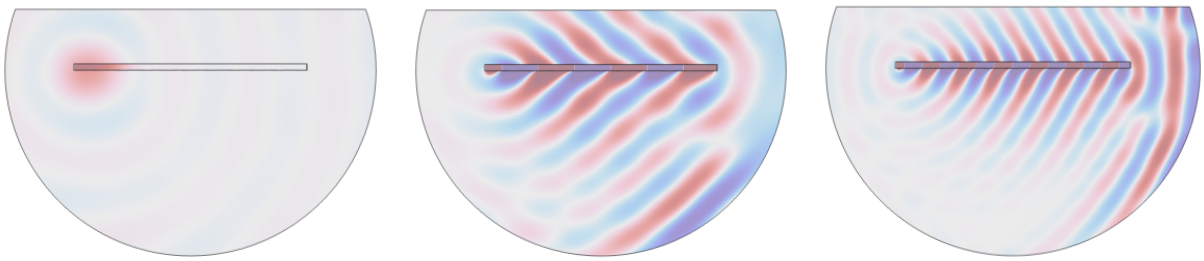

(a) $f = 600$ Hz

(b) $f = 1000$ Hz

(c) $f = 1500$ Hz

Figure 4.6: Pressure plots for the small antenna operated with a monopole source.

Pressure plots for the large ALWA with holes with $r = 4$ mm and $b = 30$ mm, operated with a dipole source, are shown for different frequencies in Figure 4.7. The cut-off frequency of the (1,0) mode for this antenna is about 1910 Hz. Below the cut-off of the (1,0) mode, shown in Figure 4.7a, it can be seen that a plane wave propagates inside the

waveguide corresponding to the (0,0) mode. However, the radiation from this mode is small and the pressure field outside of the antenna is similar to that of an omnidirectional source.

Figures 4.7b and 4.7c show the pressure field of the ALWA when it is operated above the cut-off of the (1,0) mode. Above this cut-off, the directionality of the radiation can be clearly seen, with the angle increasing with increasing frequency. Inside the antenna, the pressure field is split into two halves with opposite sign. This indicates that the (1,0) mode dominates the propagation inside the antenna, when operated with a dipole source.

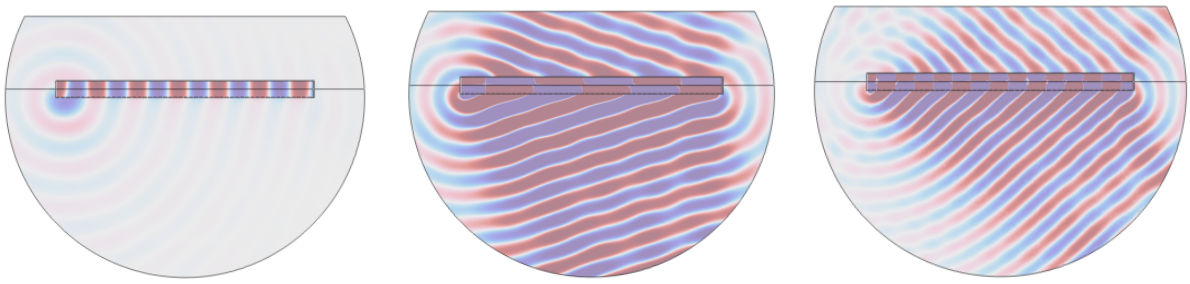

(a) $f = 1500$ Hz **(b)** $f = 2000$ Hz **(c)** $f = 2500$ Hz

Figure 4.7: Pressure plots for the large antenna operated with a dipole source.

4.2.3 Sound Pressure Level Plots

Sound pressure level (SPL) plots for the same antenna as plotted in Figure 4.6 (i.e. with a monopole excitation), with a cut-off of the (0,0) mode at about 780 Hz, are shown in Figure 4.8. At 600 Hz, it can be seen that the SPL has decayed to ambient levels about half-way through the length of the ALWA. Above the cut-off frequency, the SPL is large in a region in front of and behind the ALWA within a certain angle, which approaches endfire for higher frequencies.

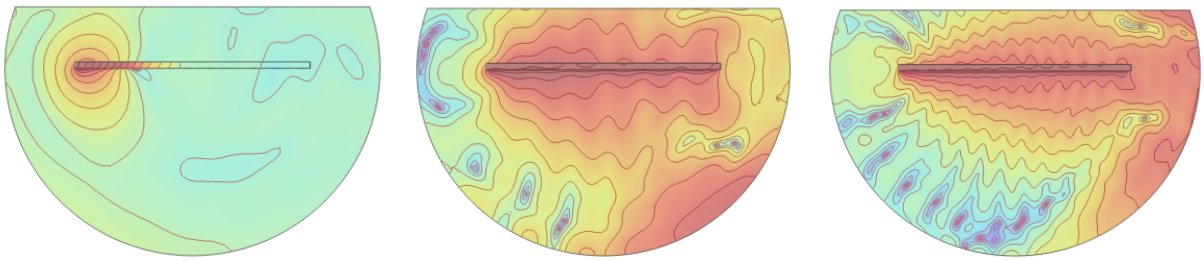

(a) $f = 600$ Hz **(b)** $f = 1000$ Hz **(c)** $f = 1500$ Hz

Figure 4.8: SPL plots for the small antenna operated with a monopole source.

SPL plots for the same antenna as plotted in Figure 4.7 (i.e. with a dipole source), with a cut-off of the (1,0) mode at about 1910 Hz, are shown in Figure 4.9. Below the cut-off of the (1,0) mode, the SPL is largest inside the cavity of the ALWA and the radiation is not very strong. Above this cut-off, there is very strong radiation, which is concentrated at particular angles, which increase with increasing frequency.

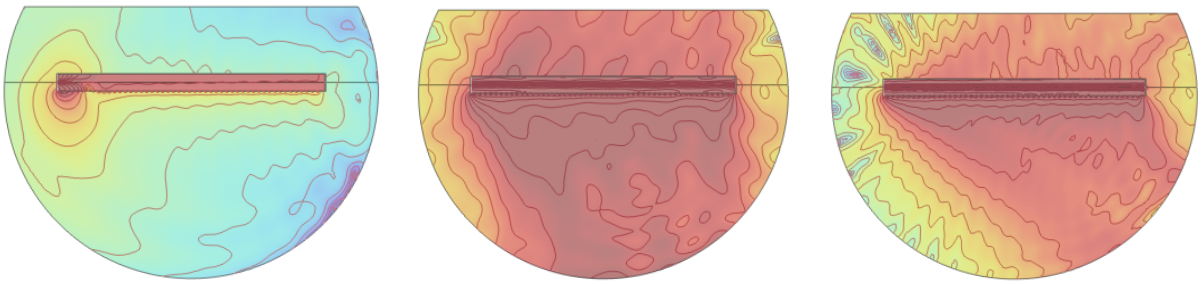

(a) $f = 1500$ Hz **(b)** $f = 2000$ Hz **(c)** $f = 2500$ Hz

Figure 4.9: SPL plots for the large antenna operated with a dipole source.

4.3 Comparison of the Theory and the Comsol Simulations

For the figures shown in this section, the radiation angles predicted by the theory and simulated in Comsol are shown in the top graph, plotted as a function of frequency. The bottom graph depicts the active component of the leakage factor predicted by the theory and simulated in Comsol, normalized by $k_0 = \omega/c$.

4.3.1 ALWA with a Slit

(0,0) Mode

The results of the Comsol simulation and the theory model for the small antenna with a slit operated in the (0,0) mode are compared in Figure 4.10 for various slit heights. There is good agreement in the radiation angle between the simulation and the theory at high frequencies, however, as the frequency approaches the cut-off frequency and below, the radiation angle predicted by the theory is much higher than the result of the simulation.

The leakage factor predicted by the theory is also much higher than the value estimated from the Comsol results for all frequencies above the cut-off frequency. Below the cut-off frequency, the theory and simulation results have opposite trends, wherein the theory trends downwards with decreasing frequency, while the simulation results trend upwards. This may be due to the method used to estimate the leakage factor from the Comsol results. As shown in the SPL plot in Figure 4.8a, the SPL at the termination has decayed to the noise floor at the measurement point close to the termination for frequencies below

the cut-off frequency. Hence, the estimation of the leakage factor becomes no longer accurate.

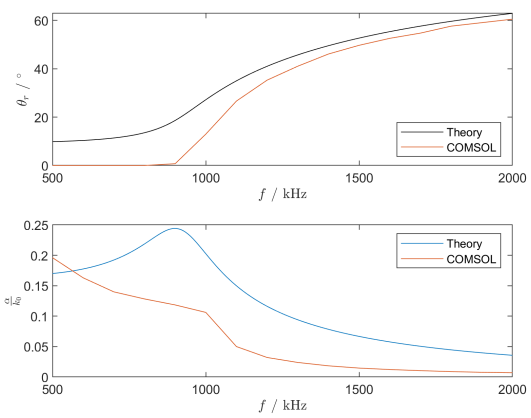

(a) $H_S = 1$ mm

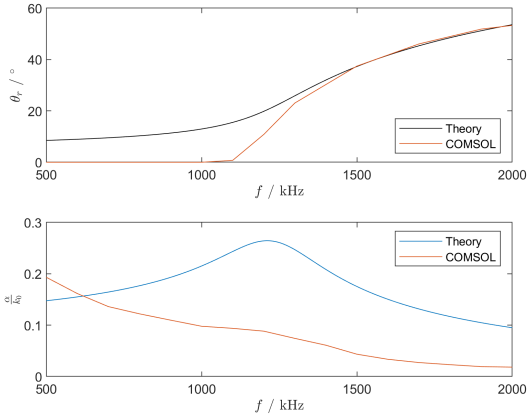

(b) $H_S = 3$ mm

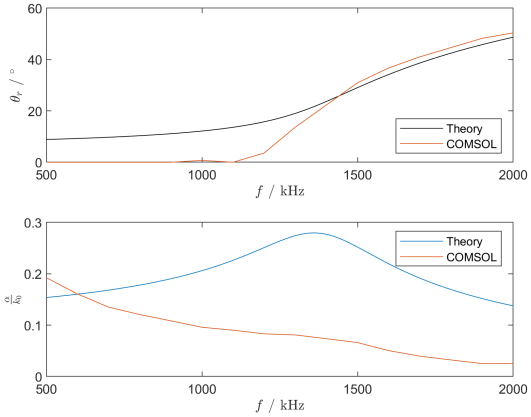

(c) $H_S = 5$ mm

Figure 4.10: Results of the Comsol simulation compared to the theoretical model for the ALWA with a slit operated in the (0,0) mode for different slit heights H_S.

(1,0) Mode

The results of the Comsol simulation and the theory model for the large antenna with a slit operated in the (1,0) mode are compared in Figure 4.11 for various slit heights. There is good agreement in the radiation angle between the simulation and the theory at all frequencies. The radiation angle deviates slightly below the cut-off, but not as much as in the case of the (0,0) mode.

The leakage factor predicted by the theory agrees closely with the simulation results at high frequencies, but deviates significantly at frequencies close to the cut-off frequency. Below the cut-off, the leakage factor seems to decrease with decreasing frequency, as predicted by the theory. This difference from the (0,0) mode simulation may be because below the cut-off for the (1,0) mode, a wave propagates in the (0,0) mode inside the antenna even when this is operated by a dipole source, whereby the power at the termination is above the noise floor and can be estimated correctly.

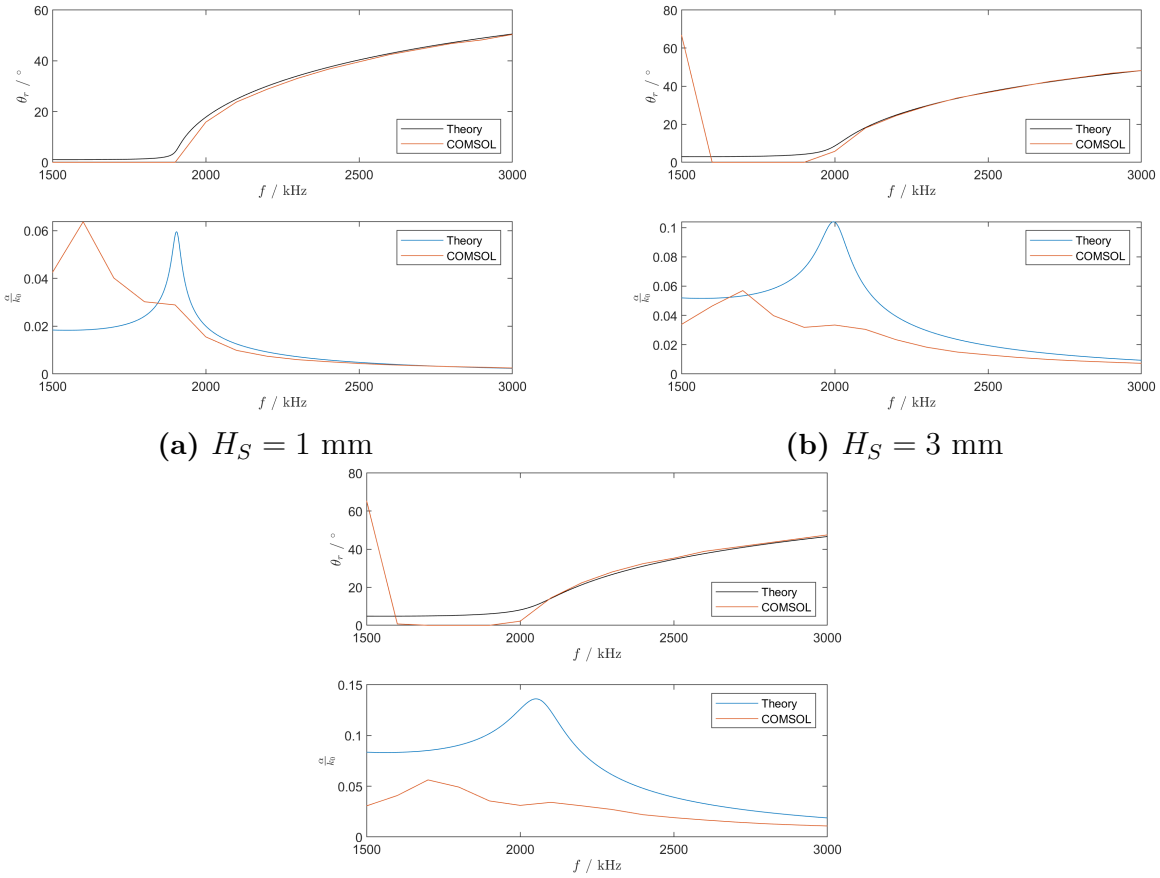

(a) $H_S = 1$ mm

(b) $H_S = 3$ mm

(c) $H_S = 5$ mm

Figure 4.11: Results of the Comsol simulation compared to the theoretical model for the ALWA with a slit operated in the (1,0) mode for different slit heights H_S.

4.3.2 ALWA with Circular Holes

(0,0) Mode

The results of the Comsol simulation and the theory model for the small antenna with circular holes operated in the (0,0) mode are compared in Figure 4.12 for various hole radii and hole separations.

The theoretical model and Comsol simulation show good agreement for all of the considered dimensions, particularly for the radiation angle. The agreement is less good for the leakage factor, but it is satisfactory above the cut-off frequency. Below the cut-off, the leakage factor is observed to increase with decreasing frequency in the Comsol model but the opposite is predicted by the theory. This may be due to the estimation method for the leakage factor in Comsol as discussed for the slit ALWA.

It can be seen that the error between the theory model and the Comsol simulation increases when the hole separation is decreased and/or the radius is increased. This suggests that there is an error in the function used to model the hole interaction since this is stronger when the holes are large or more closely spaced.

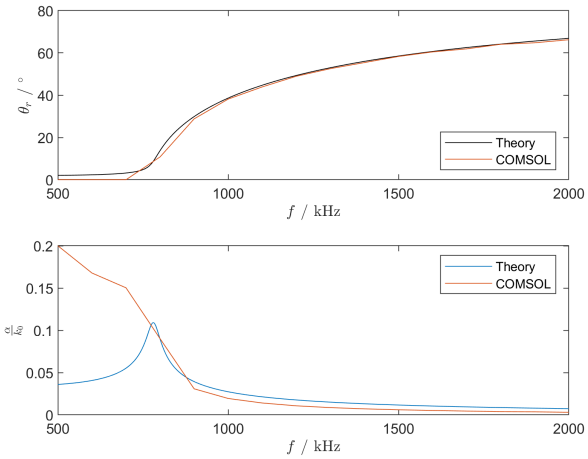

(a) $r = 2$ mm, $b = 15$ mm

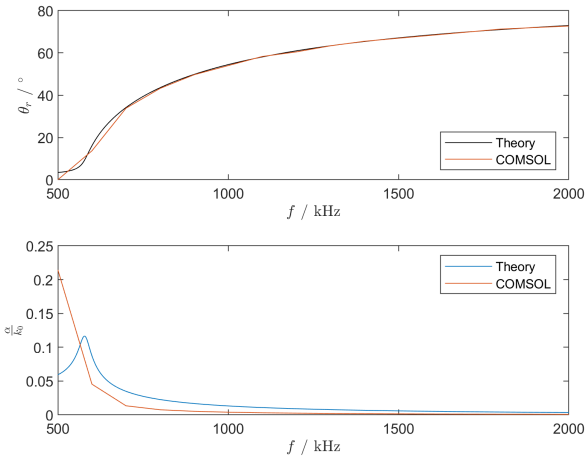

(b) $r = 2$ mm, $b = 30$ mm

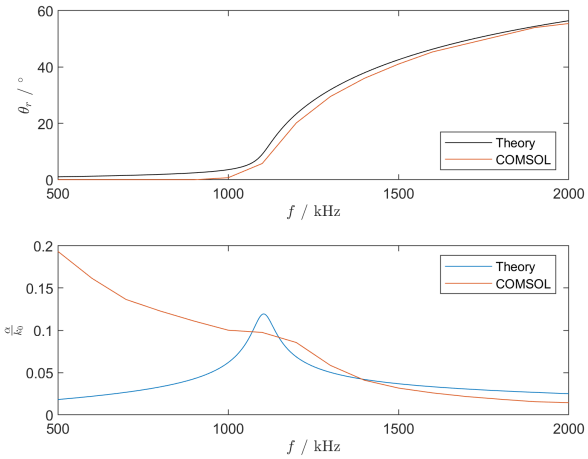

(c) $r = 4$ mm, $b = 15$ mm

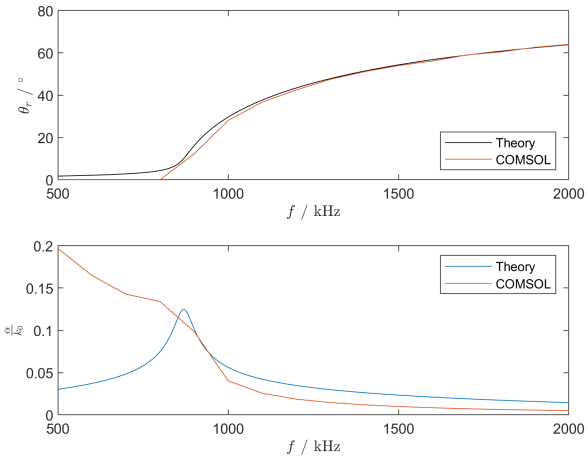

(d) $r = 4$ mm, $b = 30$ mm

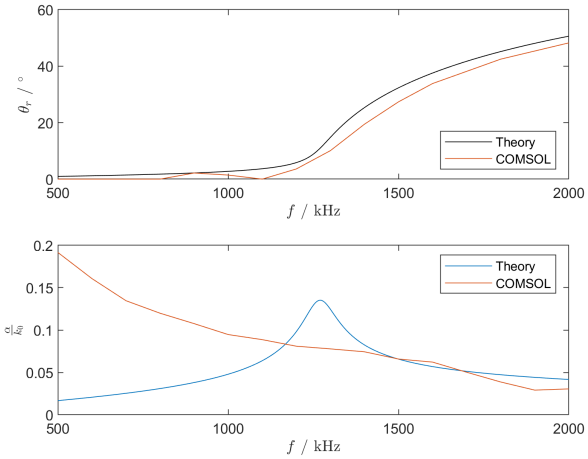

(e) $r = 6$ mm, $b = 15$ mm

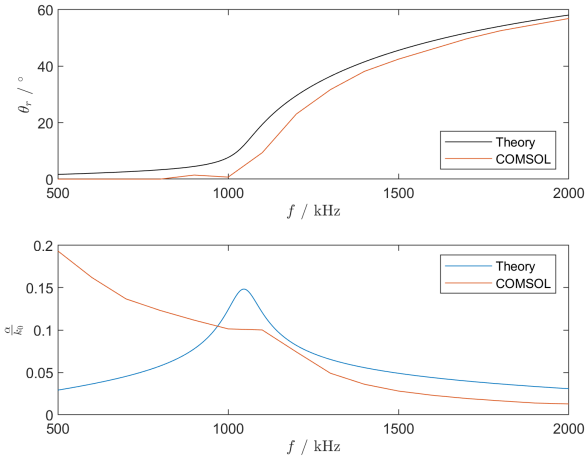

(f) $r = 6$ mm, $b = 30$ mm

Figure 4.12: Results of the Comsol simulation compared to the theoretical model for the ALWA with circular holes operated in the (0,0) mode for different radii, r, and hole separations, b.

(1,0) Mode

The results of the Comsol simulation and the theory model for the large antenna with circular holes operated in the (1,0) mode are compared in Figure 4.13 for various hole radii and hole separations. At some frequency below the cut-off frequency, the simulation results of the radiation angle show a jump to around 70°. This is because the radiation from the (1,0) mode is so small at these low frequencies that the lobe due to the (0,0) mode is detected even though the system has very little excitation in this mode due to the dipole source.

The theory model and the Comsol simulation show very good agreement for all of the dimensions tested. The opposite trends of the leakage factor below the cut-off frequency for the simulation and the theory noted for the (0,0) mode is not observed in the results for the (1,0) mode.

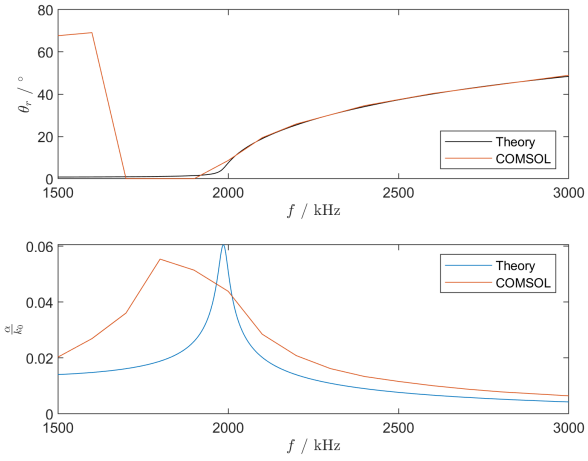

(a) $r = 4$ mm, $b = 15$ mm

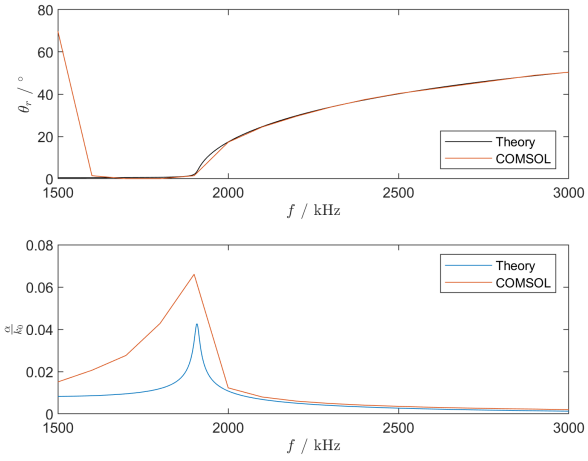

(b) $r = 4$ mm, $b = 30$ mm

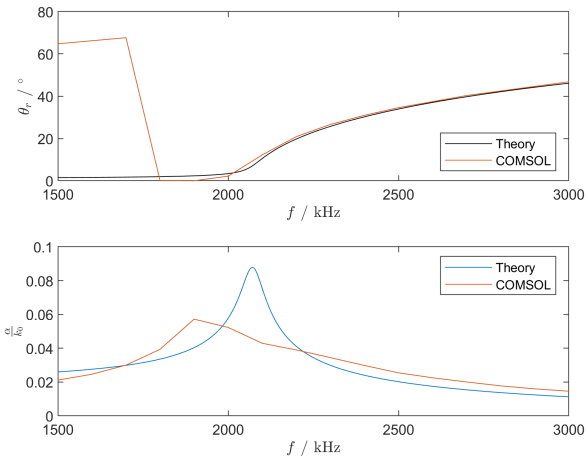

(c) $r = 6$ mm, $b = 15$ mm

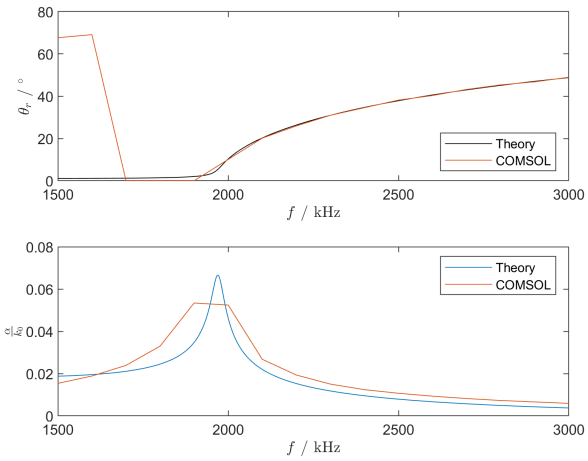

(d) $r = 6$ mm, $b = 30$ mm

Figure 4.13: Results of the Comsol simulation compared to the theoretical model for the ALWA with circular holes operated in the (1,0) mode for different radii, r, and hole separations, b.

4.4 Discussion on the effect of different dimensions on the behavior of the ALWA

The parameters that affect the properties of the ALWA according to the theoretical model are the same parameters as shown in Table 3.1, excluding the slit/hole offset and the ALWA length. The effect of changing these parameters, a predicted by the theoretical model is demonstrated in this section.

Initial dimensions were chosen as

$$H = 16 \text{ mm}, \quad W = 46 \text{ mm}, \quad d = 2 \text{ mm}, \quad H_S = 3 \text{ mm}, \quad r = 4 \text{ mm}, \quad b = 30 \text{ mm},$$

then, one dimension was changed at a time to evaluate its effect.

4.4.1 Dimensions of the Radiating Orifice

Slit Height

Figure 4.14 shows the effect of changing the slit height on the radiation angle and the leakage factor of a slit ALWA. Increasing the slit hight results in the cut-off frequency increasing and a higher leakage factor. The curve of the radiation angle also flattens out for frequencies close to the cut-off frequency.

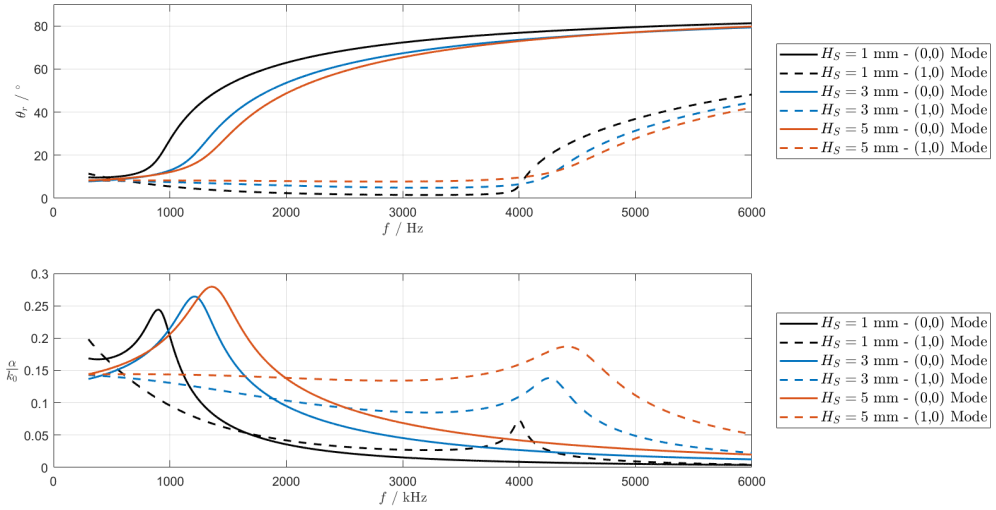

Figure 4.14: Parameter study of the slit height.

Wall Thickness

Figure 4.15a shows the effect of changing the wall thickness on the radiation angle and the leakage factor of a slit ALWA. Changing the wall thickness does not influence the results a lot. Decreasing this parameter results in a slight flattening of the radiation angle curve near the cut-off frequency and a small increase in the cut-off frequency. Increasing the wall thickness also results in a slightly smaller leakage factor.

The effect of the wall thickness on the ALWA with circular holes is shown in Figure 4.15b. Similar to the case of the slit ALWA, this parameter does not affect the radiation angle or the leakage factor very much.

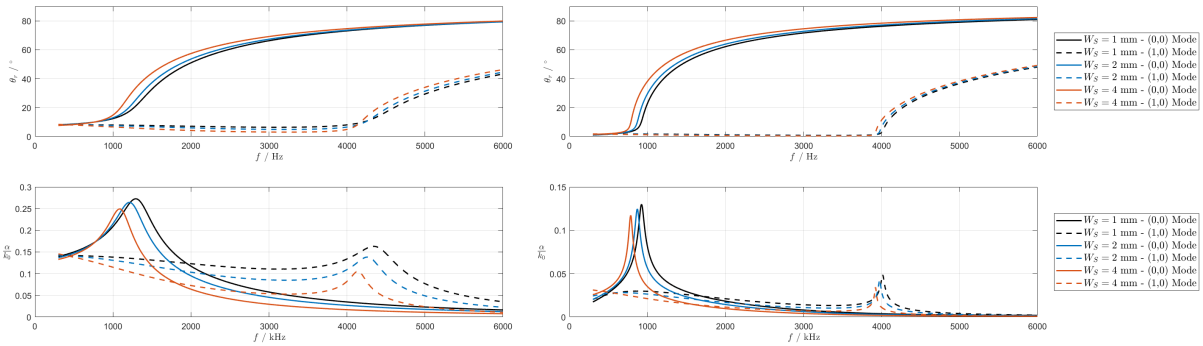

(a) Slit ALWA. **(b)** ALWA with circular holes.

Figure 4.15: Parameter study of the wall thickness.

Hole Radius

Figure 4.16 shows the effect of changing the hole radius on the radiation angle and the leakage factor of a ALWA with circular holes. Increasing the radius of the holes shifts the cut-off frequency upwards significantly. ALWAs with a small hole radius have a smaller leakage factor and a steeper increase in the radiation angle for frequencies close to the cut-off frequency.

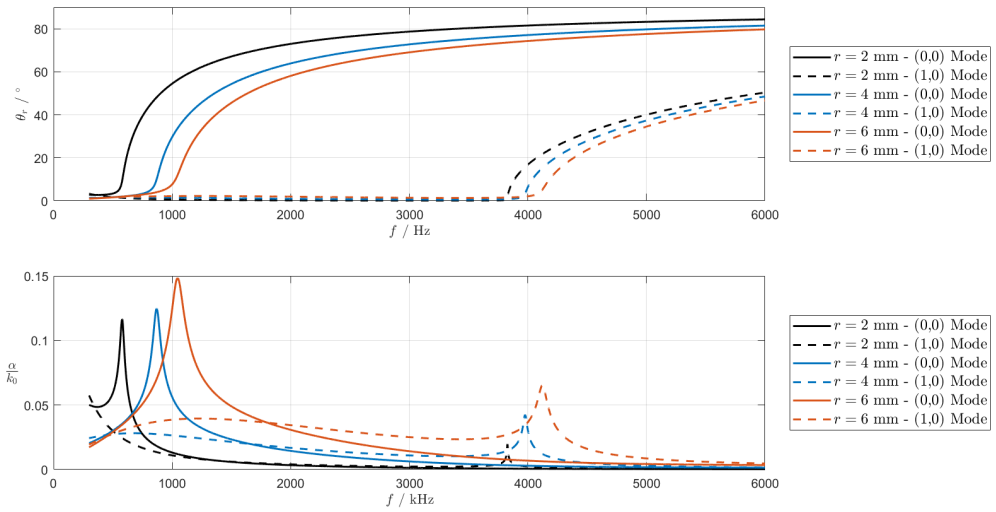

Figure 4.16: Parameter study of the hole radius.

Hole Separation

The effect of the hole separation on ALWAs with circular holes is shown in Figure 4.17. It can be seen that increasing the hole separation causes the cut-off frequency to decrease.

The leakage factor is not affected a lot for the (0,0) mode, however, reducing the hole separation increases the leakage factor for the (1,0) mode. It should be noted, however, that at high frequency the hole separation is limited by the wavelength, since it must be significantly shorter than this.

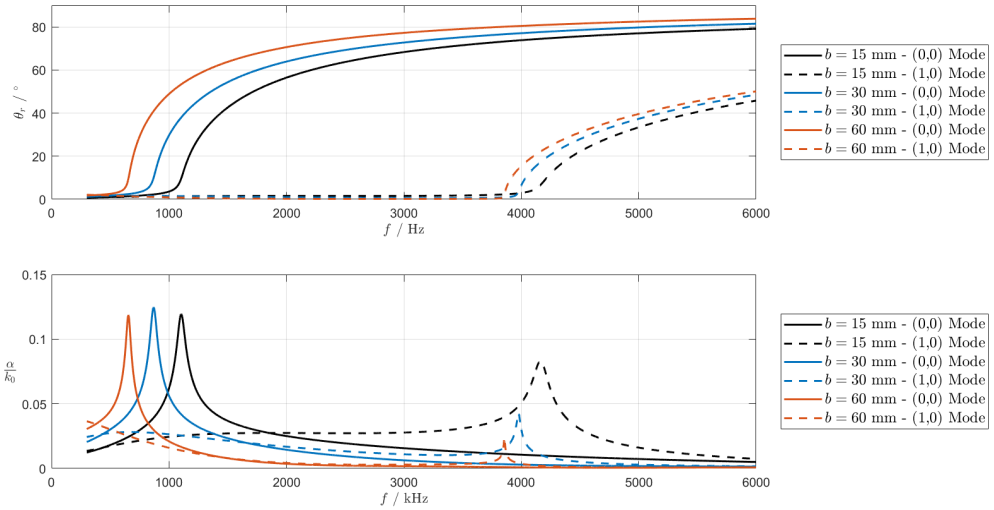

Figure 4.17: Parameter study of the hole separation.

4.4.2 Dimensions of the ALWA Cavity

Cavity Height

The effect of the cavity height on the slit ALWA and the ALWA with circular holes is shown in Figure 4.18. In both cases, increasing the height causes the cut-off frequency to decrease. The leakage factor shows opposite trends for the two different modes, increasing with the height for the (0,0) mode, but decreasing for the (1,0) mode.

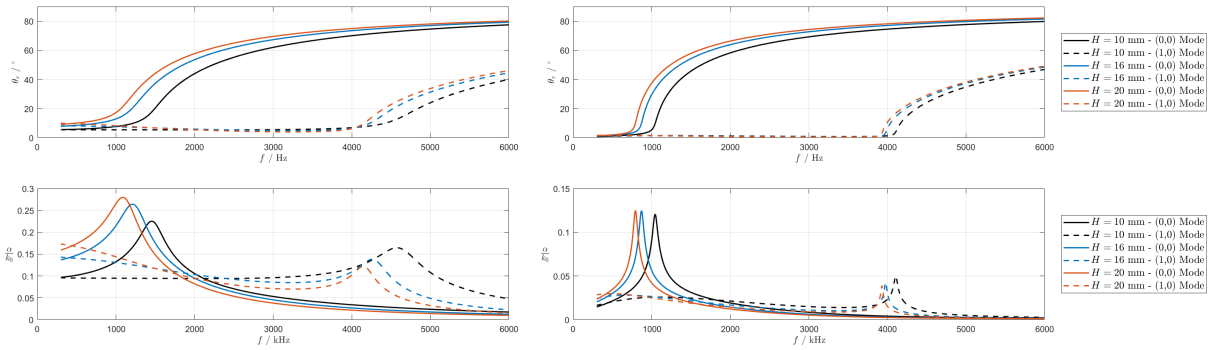

(a) Slit ALWA. **(b)** ALWA with circular holes.

Figure 4.18: Parameter study of the cavity height.

Cavity Width

Since the ALWA width does not feature in the equations for the impedance of the slit or the holes, this parameter should affect both types of ALWA in a similarly. Figure 4.19 shows the effect of the cavity width on the ALWA with circular holes. It is clear that the width has a large influence on the cut-off frequency of the (1,0) mode, but a much smaller influence on the cut-off of the (0,0) mode. For both modes, increasing the width causes the cut-off frequency to decrease.

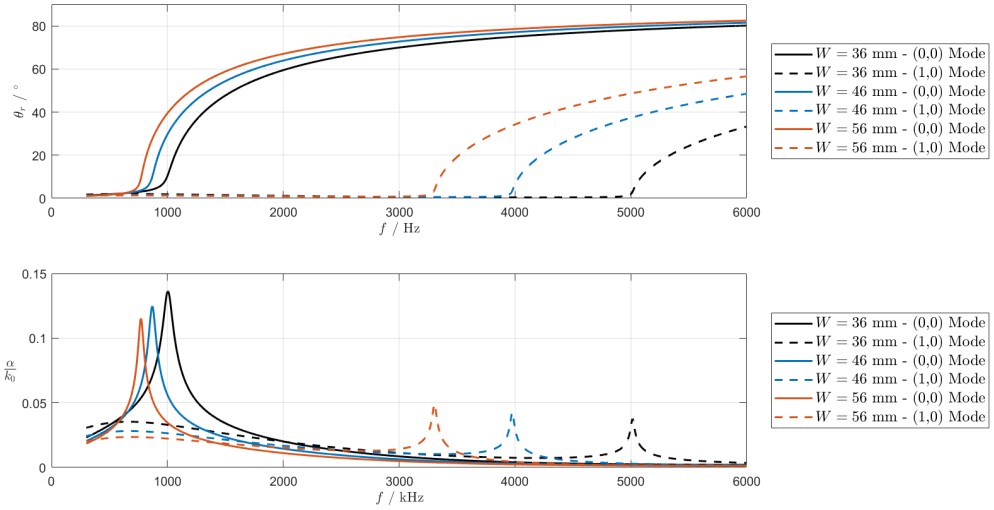

Figure 4.19: Parameter study of the cavity width for the ALWA with circular holes.

4.5 Comparison with the Radiation Angle and Leakage Factor from the Experimental Measurements

The radiation angle and leakage factor were calculated from the experimental measurements. The radiation angle was calculated from the measurements of the directivity with an absorber termination while the leakage factor was calculated from the measurements with a reflector termination using Eq. (3.4). The results presented in this section are the average values of these parameters calculated from the measurements in four different microphone positions. The uncertainty shown in the graphs in this section was calculated according to Eq. (3.5).

4.5.1 Large Antenna

Monopole Source

The results of the radiation angle and leakage factor for the large antenna operated with a monopole source compared to the results of the theoretical model and the Comsol simulations are shown in Figures 4.20 and 4.21 respectively. There is good agreement between the measurements, simulations and theory in frequencies above 1500 Hz and below about 1000 Hz. However, for a small frequency range around 975 Hz, the measured

results deviate to a large extent from the simulation and the theory. This deviation is likely due to a resonance within the antenna. The leakage factor agrees closely with the theory, particularly for frequencies above around 1300 Hz. Below this frequency, the measured value of α is slightly higher between 1000 Hz and 1300 Hz and slightly lower below 1000 Hz.

Furthermore, for frequencies below 1000 Hz, deviations with large discrepancies between the four measurements (as indicated by the large error bars) occur at periodic intervals of about 100 Hz. The length of the large antenna was primarily designed for operation in the (1,0) mode, with frequencies above 1500 Hz. Therefore, at lower frequencies, the length of the antenna may be only a few wavelengths, which could disturb the ALWA's operation. The deviations at multiples 100 Hz may correspond to resonances along the length of the ALWA caused by waves which are not sufficiently absorbed by the termination and reflected, forming a standing wave pattern.

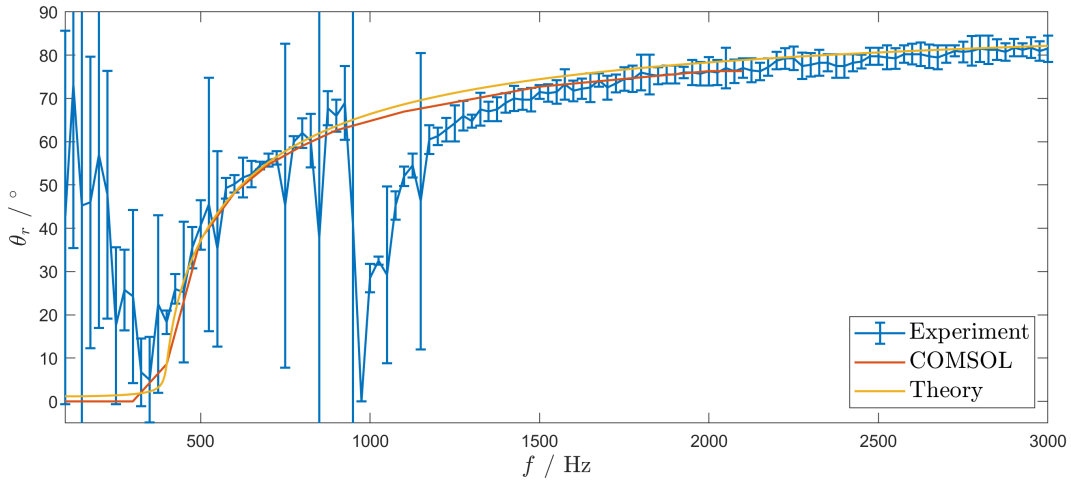

Figure 4.20: Comparison of the measured radiation angle with the Comsol simulation and the theoretical model for the large ALWA operated with a monopole source.

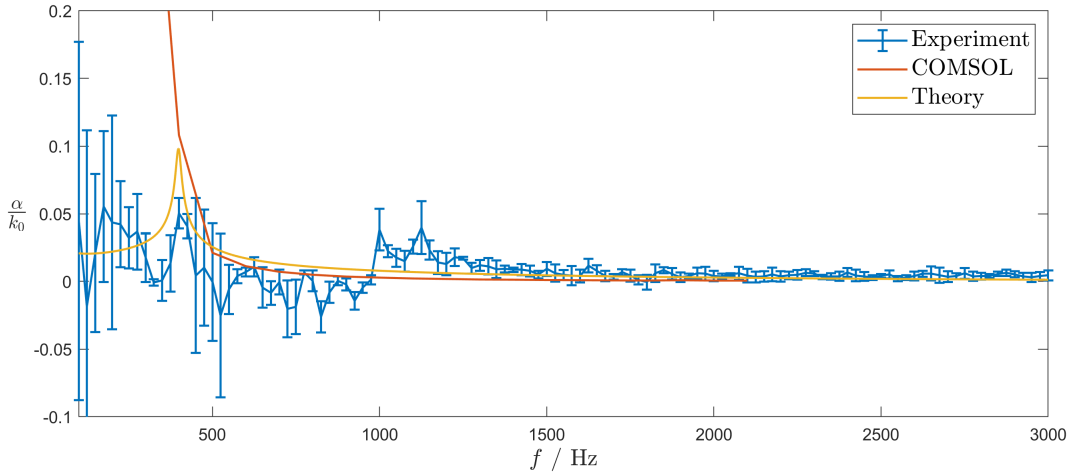

Figure 4.21: Comparison of the measured leakage factor with the Comsol simulation and the theoretical model for the large ALWA operated with a monopole source.

Dipole Source

The results of the radiation angle and leakage factor from the experimental measurement of the large antenna operated with a dipole source are shown in Figures 4.22 and 4.23 respectively. Very good agreement is observed between the theory, Comsol simulation and measurements for the radiation angle at all frequencies above the cut-off frequency. The measured leakage factor was slightly higher than predicted by the theory and the simulation.

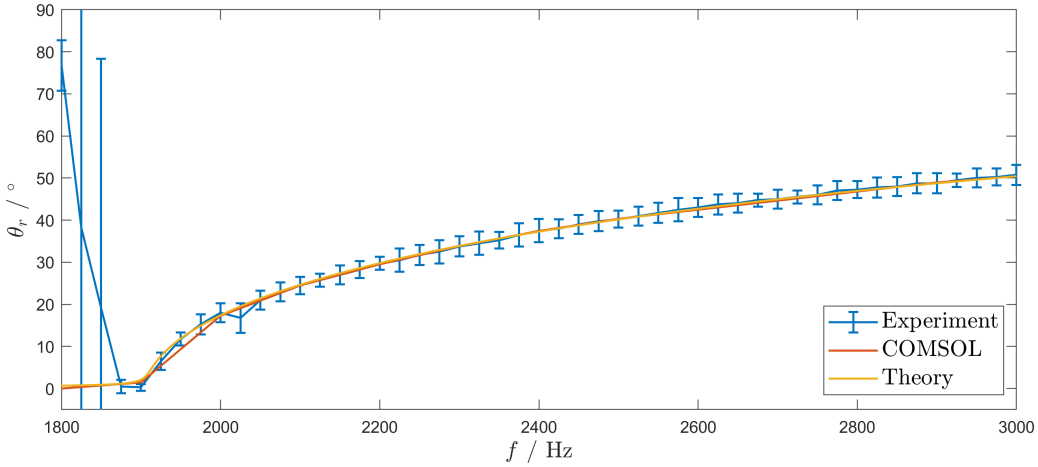

Figure 4.22: Comparison of the measured radiation angle with the Comsol simulation and the theoretical model for the large ALWA operated with a dipole source.

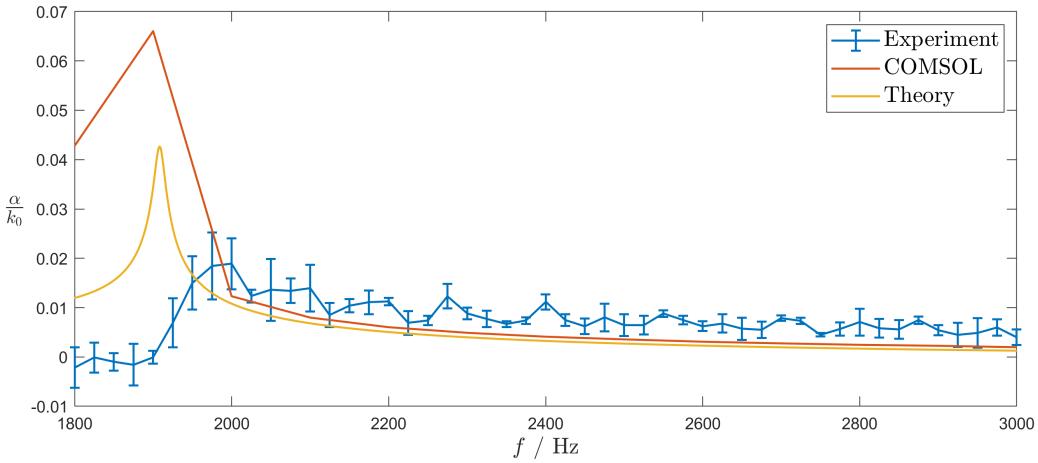

Figure 4.23: Comparison of the measured leakage factor with the Comsol simulation and the theoretical model for the large ALWA operated with a dipole source.

4.5.2 Small Antenna

Monopole Source

Figures 4.24 and 4.25 show the results of the experimental measurement of the small ALWA operated with a monopole source. Both the measured radiation angle and the leakage factor demonstrate good agreement with the theory and FEM simulation, except

in a small frequency range at about 2050 Hz. In this range, there are large discrepancies between the measurements at different positions as indicated by the large error bars. This is similar to the deviation observed for the large antenna operated by a monopole source, but the frequency range is shifted upwards. This suggests that this effect may be dependent on the width of the ALWA cavity.

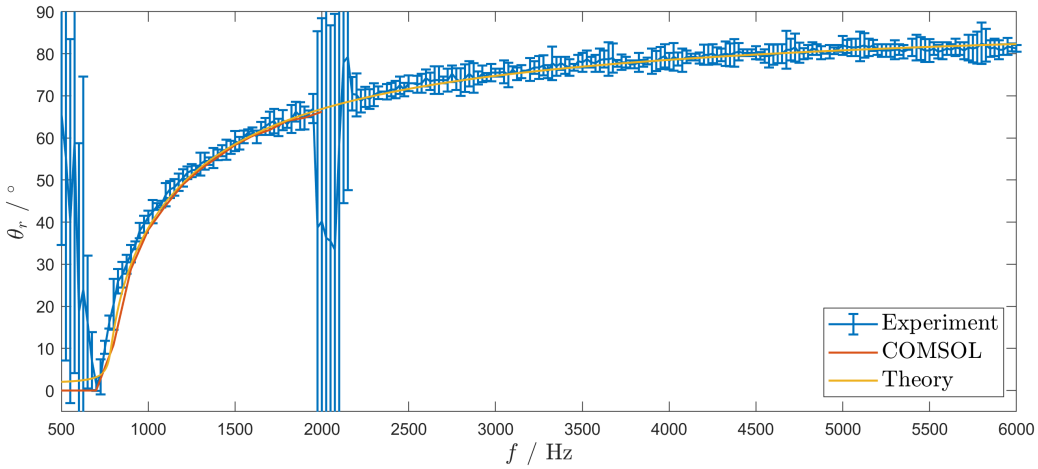

Figure 4.24: Comparison of the measured radiation angle with the Comsol simulation and the theoretical model for the small ALWA operated with a monopole source.

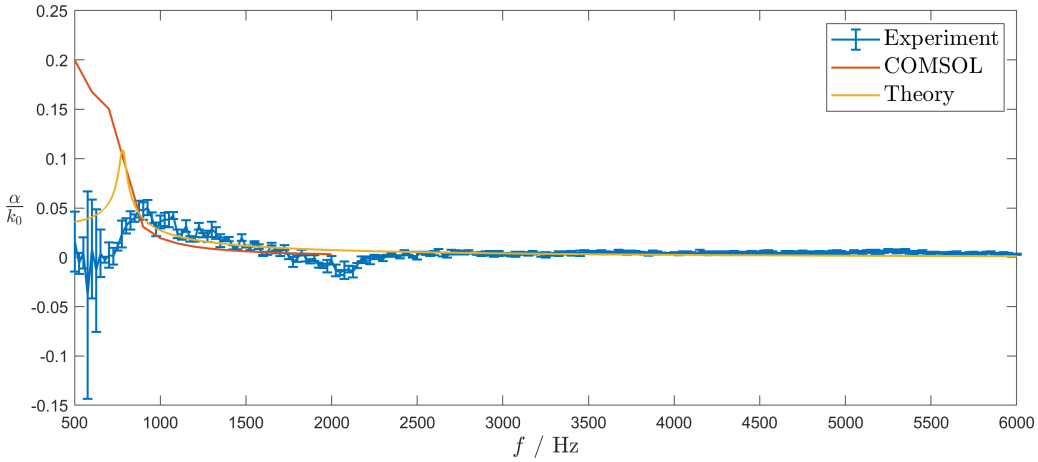

Figure 4.25: Comparison of the measured leakage factor with the Comsol simulation and the theoretical model for the small ALWA operated with a monopole source.

Dipole Source

The results of the experimental measurements for the small ALWA operated by a dipole source are shown in Figures 4.26 and 4.27. The results show poor agreement with the theory for both the radiation angle and the leakage factor. The radiation angle follow similar trends, but the theory is about 5° higher than the measured angle for all frequencies. The constant offset means that it may be possible that the ALWA is effectively not radiating from the center but at a location closer to the source. A 5° offset corresponds to radiation from a quarter of the total length at 0°. The location of the source of radiation which

produces an offset of 5° moves towards the source as θ_r increases. The measured leakage factor is much higher than predicted by the theory. This might be because most of the power inside the ALWA was radiated before being reflected at the termination.

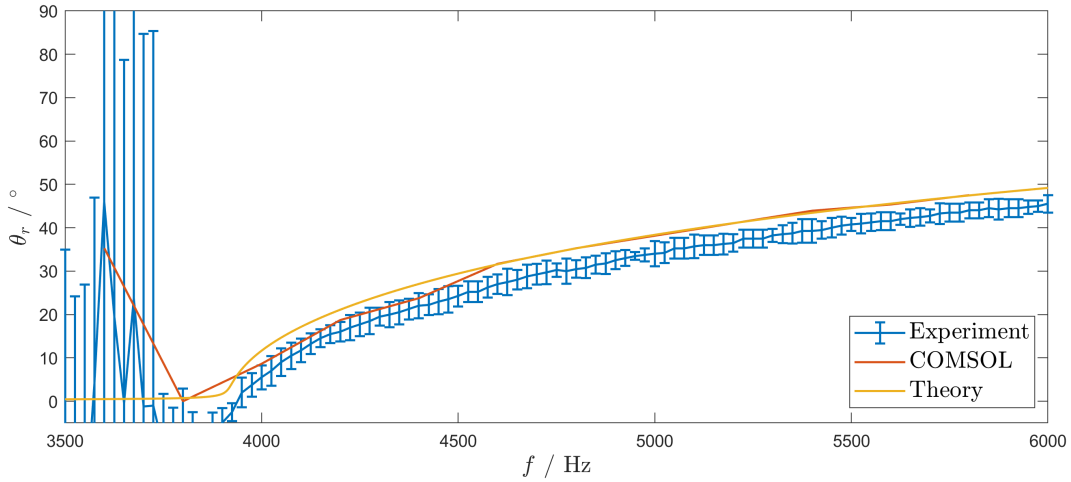

Figure 4.26: Comparison of the measured radiation angle with the Comsol simulation and the theoretical model for the small ALWA operated with a dipole source.

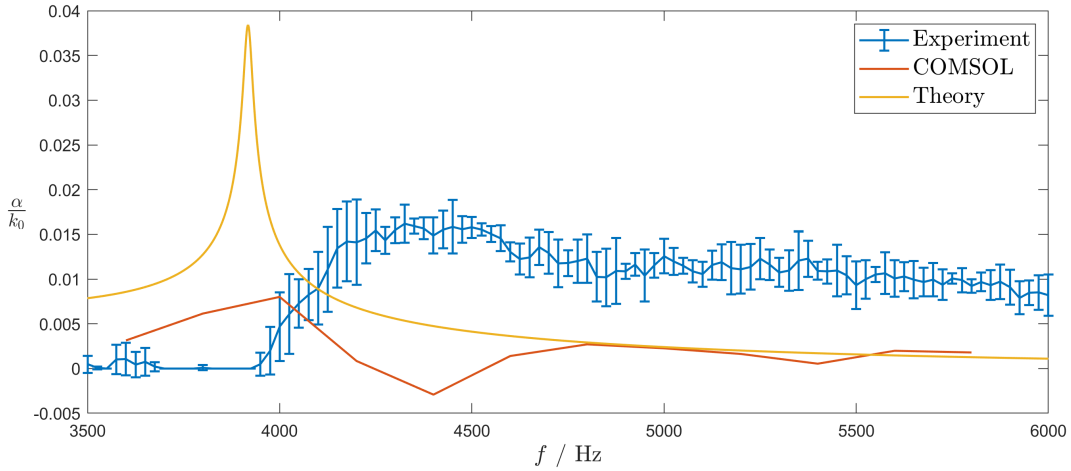

Figure 4.27: Comparison of the measured leakage factor with the Comsol simulation and the theoretical model for the small ALWA operated with a dipole source.

4.6 Directivity Plots of Experimental Results

To investigate the results of the experimental measurements further, directivity plots can be made to show the whole measurement in a single figure using a 2D surface plot and to observe the directivity pattern at particular frequencies using polar plots. The theoretically predicted radiation angle is plotted in black on the 2D surface plots. The plots shown in this section are taken from the measurements taken in Position 1 (for the large ALWA) and Position 5 (for the small ALWA). The estimated uncertainty of these plots is the same as the uncertainty of the initial angle of the microphone position from Table 3.3.

4.6.1 Large Antenna

Monopole Source

Figure 4.28 shows the 2D surface directivity plots for the large ALWA operated with a monopole source. It can be seen that the radiation of the ALWA generally follows the trend predicted by the theory. In a narrow band around 1000 Hz, the radiation goes to broadside and increases back to the predicted angle. Beyond the cut-off frequency of the (1,0) mode, a side-lobe that follows the trend of the theoretically predicted radiation of this mode appears. It can be seen that when the reflector termination is used, the radiation increases and decreases with a period of about 100 Hz. This likely corresponds to the resonance along the length of the ALWA. This periodicity can also be observed for the measurement with the absorber termination, however, the effect is less pronounced in this case.

The resonance of a quarter-wave resonator (a closed-open pipe) along the width of the ALWA can be calculated as:

$$f_r = \frac{c}{4W} = \frac{343 \text{ m s}^{-1}}{4 \times 0.095 \text{ m}} = 903 \text{ Hz}. \tag{4.1}$$

This frequency is lower than the frequency of the disturbance, but it is rather close.

The resonance of a half-wave resonator (a closed-closed pipe) along the length of the ALWA can be calculated as:

$$f_r = \frac{c}{2L} = \frac{343 \text{ m s}^{-1}}{2 \times 1.5 \text{ m}} = 114 \text{ Hz}. \tag{4.2}$$

This is consistent with the periodic fluctuations of the radiated sound power observed in the case of the reflector termination.

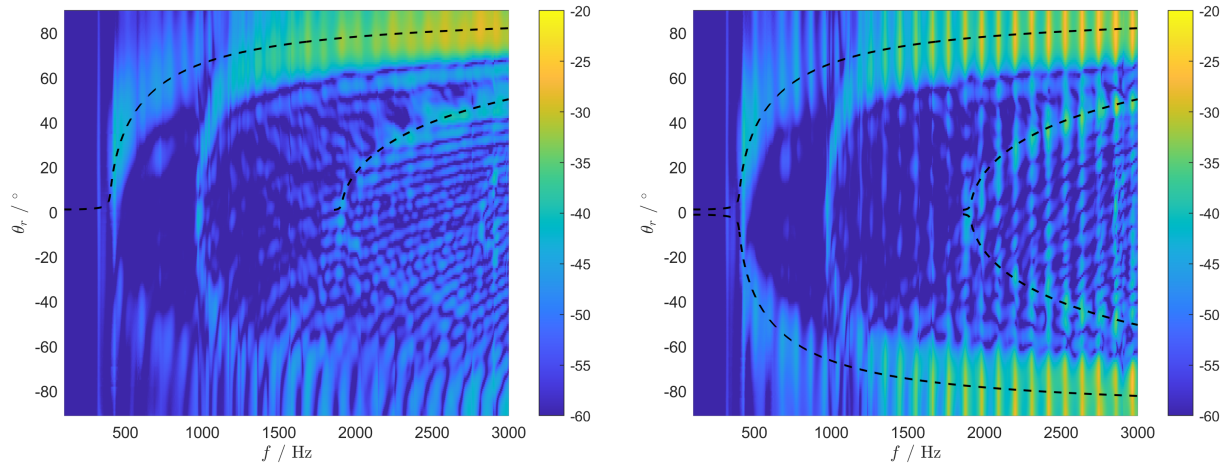

(a) Absorber **(b)** Reflector

Figure 4.28: 2D-surface directivity plot for the experimental measurement of the large antenna operated with a monopole source

The corresponding polar plots of the directivity are shown in Figure 4.29. Figure 4.29a shows that below the cut-off frequency of the (0,0) mode, there is no discernible radiation

pattern, with many random spikes in the measurement. At 300 Hz, closer to the cut-off frequency, the radiation seems to be approximately omnidirectional. Once the cut-off of the (0,0) mode is exceeded, distinct lobes become visible as shown in Figure 4.29b. At the frequency range of the deviation from the theory, shown in Figure 4.29c, it can be seen that there is a strong lobe that forms at broadside, whose radiation angle increases quickly with frequency, approaching the predicted angle. Above the cut-off of the (1,0) mode, as shown in Figure 4.29d, the side-lobes corresponding to this mode can be clearly seen. The angle of the side-lobes increases with frequency, starting close to broadside at 1800 Hz and increasing to around 55° at 3000 Hz.

Comparing Figures 4.29b and 4.29e, it can be seen that the absorber used does not reduce the back-lobe significantly for some of the lower frequencies between 600 Hz and 900 Hz. Comparing Figures 4.29d and 4.29f considerable reduction in the back-lobe can be seen for the high frequencies above 1300 Hz.

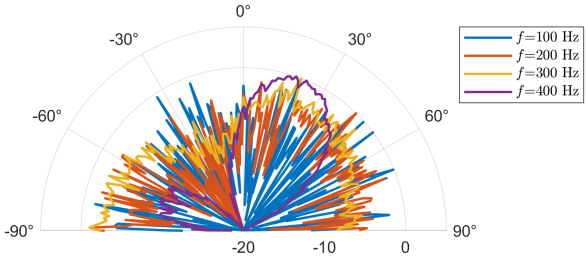

(a) Up to cut-off frequency of the (0,0) mode (Absorber)

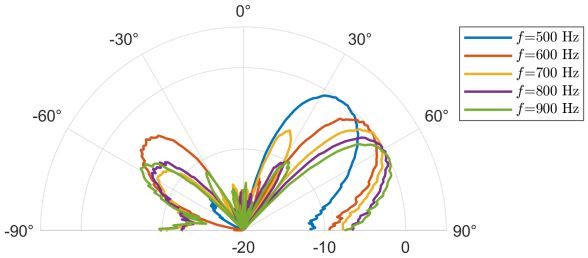

(b) Above the cut-off frequency of the (0,0) mode (Absorber)

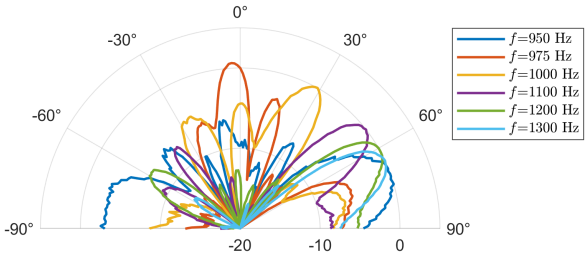

(c) Frequency Range of Deviation at around 1000 Hz (Absorber)

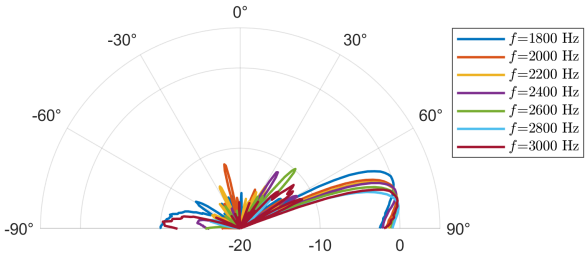

(d) Above the cut-off frequency of the (1,0) mode (Absorber)

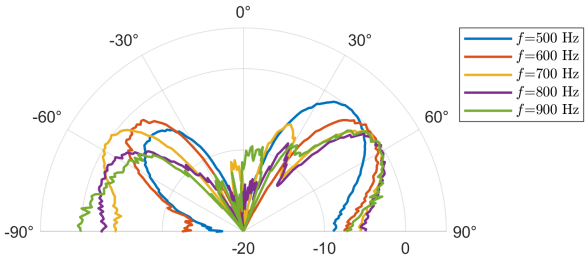

(e) Above the cut-off frequency of the (0,0) mode (Reflector)

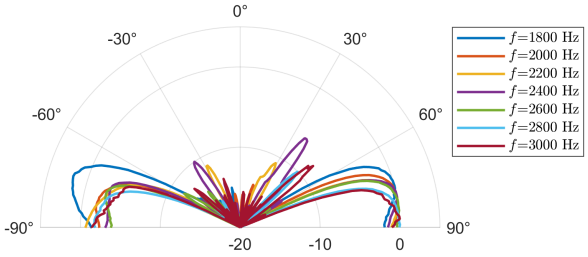

(f) Above the cut-off frequency of the (1,0) mode (Reflector)

Figure 4.29: Polar plots of the large ALWA operated with a monopole source

Dipole Source

The 2D surface directivity plots of the measurements of the large antenna operated with a dipole source with the absorber and reflector terminations are shown in Figure 4.30. These plots demonstrate good agreement between the theory and the measurements. A side lobe at about 2900 Hz can be seen at broadside, but otherwise, no prominent side lobes are visible in the plots. The measurements with the reflector demonstrate a periodic fluctuation of the measured sound pressure like in the case of the monopole source.

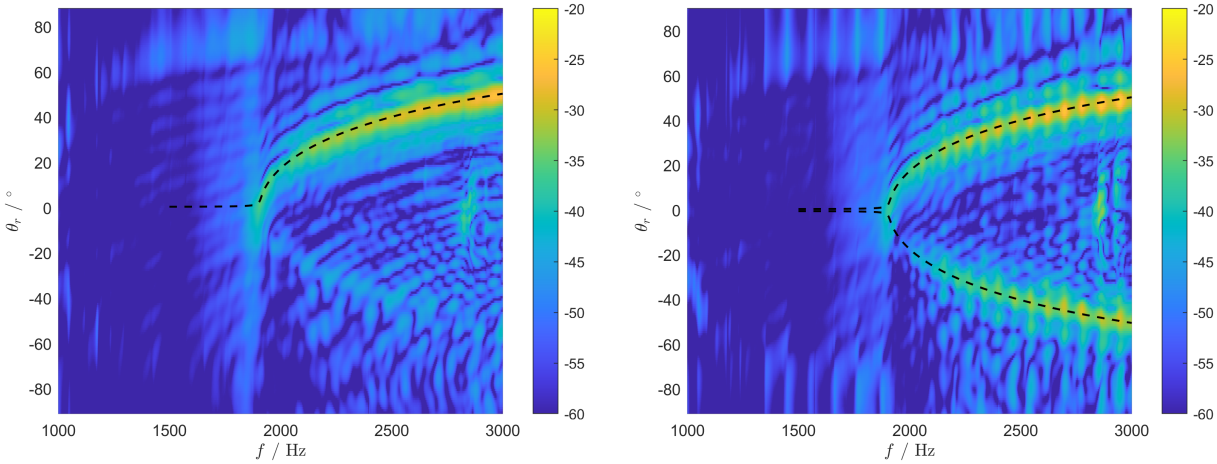

(a) Absorber **(b)** Reflector

Figure 4.30: 2D-surface directivity plot for the experimental measurement of the large antenna operated with a dipole source

The polar plots showing the directivity at select frequencies are shown for the measurements taken with the absorber and reflector terminations in Figures 4.31 and 4.32 respectively. Figure 4.31a showa that below the cut-off of the (1,0) mode, the lobe of the (0,0) mode, pointed at around 70°, is about 10 dB stronger than the radiation in the other directions, however, as the cut-off is surpassed, this lobe becomes much smaller than the lobe of the (1,0) mode as shown in Figure 4.31b.

Comparing the plots for the different terminations (Figures 4.31 and 4.32), it can be seen that the absorber significantly reduces the back-lobe at all frequencies, except at 2000 Hz.

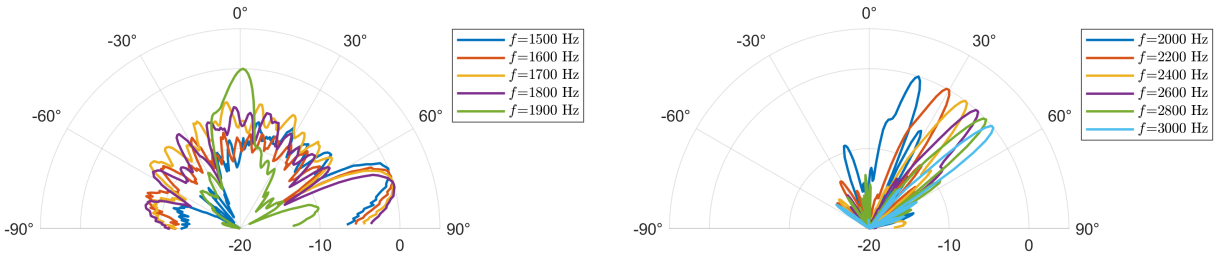

(a) Up to the cut-off of the (1,0) mode **(b)** Above the cut-off of the (1,0) mode

Figure 4.31: Directivity plots for the large ALWA prototype operated by a dipole with the absorber termination

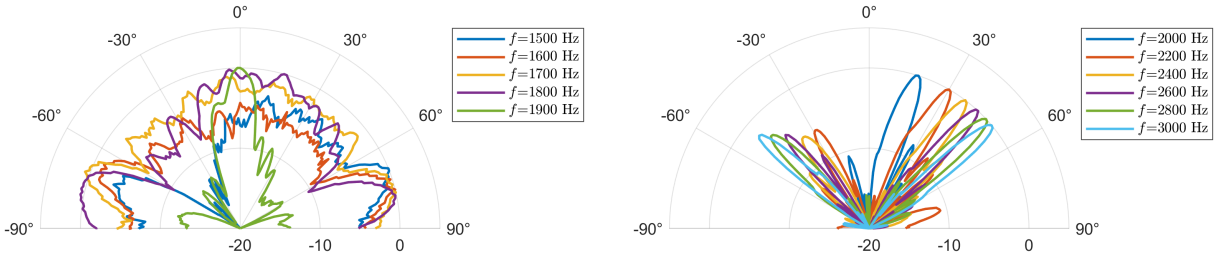

(a) Up to the cut-off of the (1,0) mode **(b)** Above the cut-off of the (1,0) mode

Figure 4.32: Directivity plots for the large ALWA prototype operated by a dipole with the reflector termination

4.6.2 Small Antenna

Monopole Source

The 2D surface plots of the measurement of the small ALWA prototype operated with a monopole source are shown in Figure 4.33. It can be seen that the radiation pattern closely follows the theoretical prediction, except at around 2000 Hz. At this frequency, the front-lobe disappears and a strong back-lobe appears instead. A side-lobe corresponding to the (1,0) mode also appears above its cut-off. An additional side-lobe appears at frequencies above 3000 Hz which is not associated with any known modes. This side-lobe does not appear to be reflected in the measurement with the reflector termination (Figure 4.33b). The periodic fluctuations in the reflector measurement are observed again. The resonance frequency for the length of the small ALWA prototype is 98 Hz.

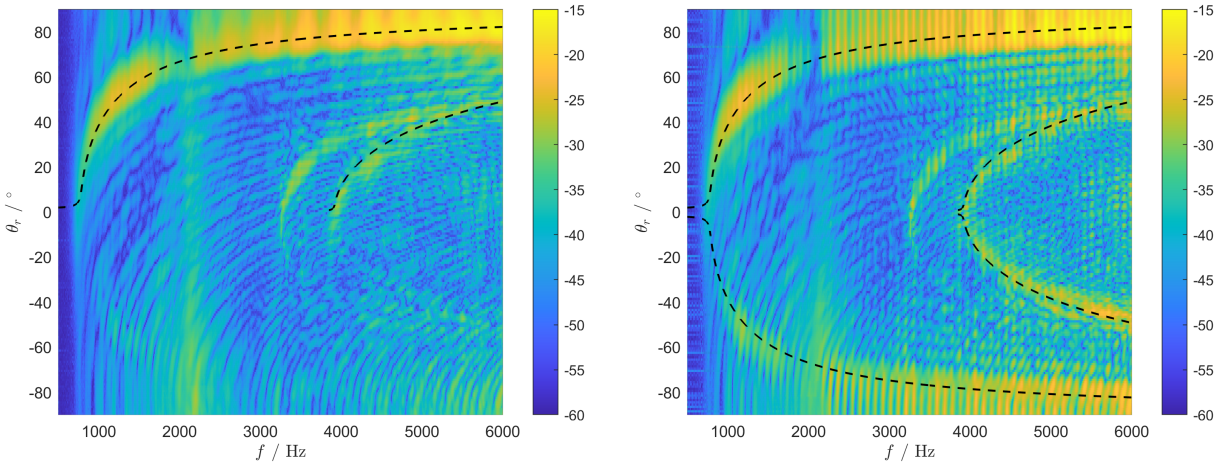

(a) Absorber **(b)** Reflector

Figure 4.33: 2D-surface directivity plot for the experimental measurement of the small antenna operated with a monopole source

The frequency of the quarter-wave resonator along the width of the small ALWA is:

$$f_r = \frac{c}{4W} = \frac{343 \text{ m s}^{-1}}{4 \times 0.046 \text{ m}} = 1864 \text{ Hz}. \tag{4.3}$$

Again, this frequency is smaller than but close to that of the observed disturbance.

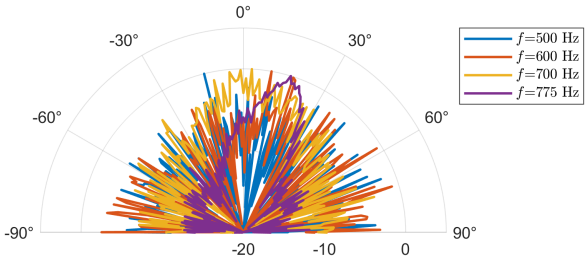

(a) Up to cut-off frequency of the (0,0) mode (Absorber)

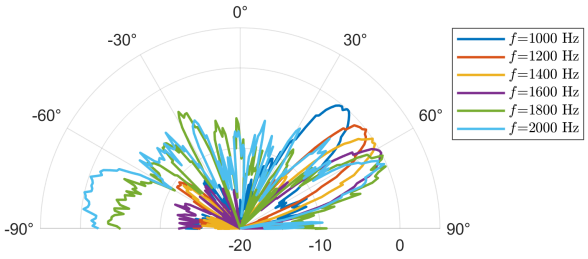

(b) Above the cut-off frequency of the (0,0) mode (Absorber)

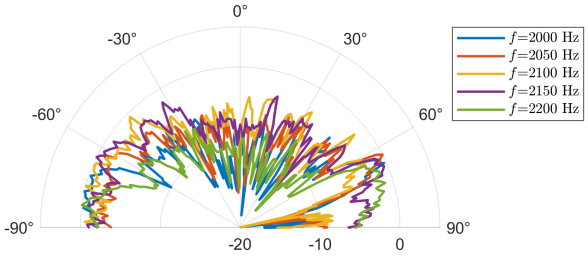

(c) Frequency Range of Deviation from Theory and Comsol (Absorber)

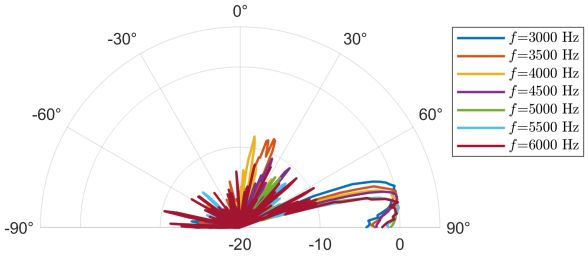

(d) Above the cut-off frequency of the (1,0) mode (Absorber)

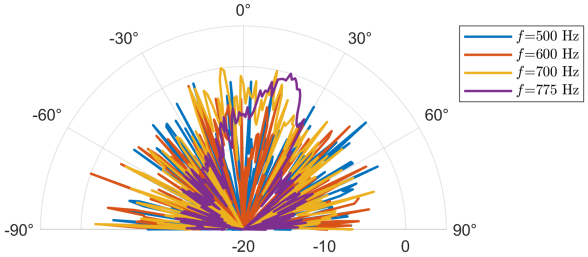

(e) Up to cut-off frequency of the (0,0) mode (Reflector)

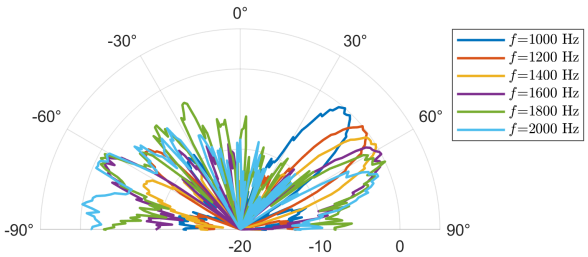

(f) Above the cut-off frequency of the (0,0) mode (Reflector)

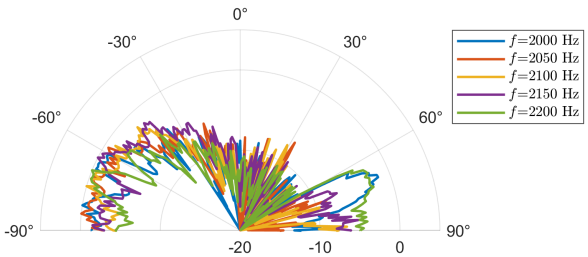

(g) Frequency Range of Deviation from Theory and Comsol (Reflector)

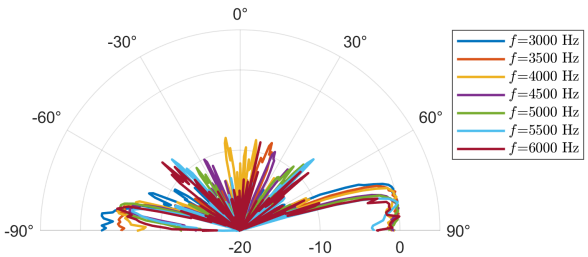

(h) Above the cut-off frequency of the (1,0) mode (Reflector)

Figure 4.34: Polar plots of the large ALWA prototype operated with a monopole source

Polar plots of the directivity for the small ALWA operated with a dipole source are shown in Figure 4.34. For most frequency ranges, similar directivity to the case of the large antenna operated with a monopole source is observed. For the small antenna, at the frequency range of the deviation, a large back-lobe is observed instead of a lobe at broadside as shown in Figure 4.34c. When the reflector termination was used, the back-

lobe was stronger than the front lobe in this frequency range (Figure 4.34g). In Figure 4.34b, the back-lobe can be seen to increase in magnitude starting from 1800 Hz with the absorber termination. The absorber significantly reduces the back-lobe at all frequencies above the cut-off (except in the range of the deviation).

Dipole Source

Figure 4.35 shows the 2D surface directivity plot of the measurements taken of the small ALWA prototype operated with a dipole source. A small shift can be seen between the theoretical prediction and the measured radiation which was not observed for the side-lobe corresponding to the (1,0) mode when operated by a monopole source. The trend of the theoretical prediction and the measurements is similar.

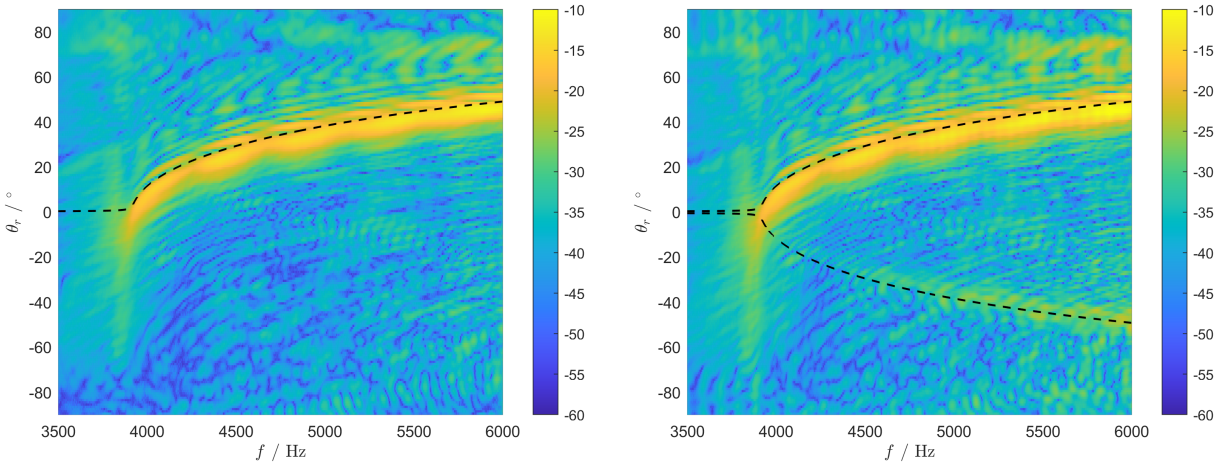

(a) Absorber **(b)** Reflector

Figure 4.35: 2D-surface directivity plot for the experimental measurement of the small antenna operated with a dipole source

The polar plots of the directivity for the small ALWA operated with a dipole source are shown in Figures 4.36 and 4.37. For the frequency just above the cutoff, it can be seen that the lobe is centered at about $-5°$. This indicates that the radiation may be occurring at a point closer to the source than the midpoint. The measurement at position 5 shown here was taken at a distance of about 5 m. This would mean that a 5° offset would correspond to radiation from a quarter of the length rather than the mid-point. The back-lobes for the measurements with the reflector termination are small, indicating that most of the power is radiated before it can be reflected.

Figure 4.38 shows the directivity measured at the different microphone positions. If the offset is due to radiation closer to the source, this should vary depending on the perpendicular distance from the center of the ALWA to the microphone. This distance is 5.15 m (Position 5), 3.37 m (Position 6), 4.4 m (Position 7) and 3.9 m (Position 8). Hence, if the offset is due to radiation closer to the source, it should be the largest for Position 6, followed by Position 8 and Position 7, with Position 5 having the smallest offset. Hence, the results of the measurements are consistent with this hypothesis.

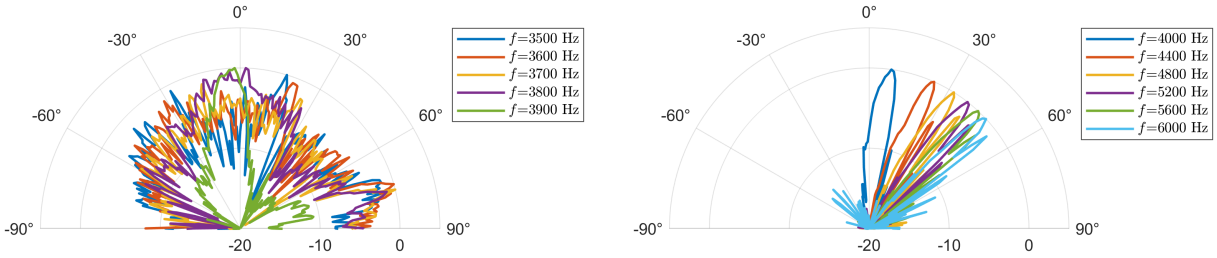

(a) Up to the cut-off of the (1,0) mode **(b)** Above the cut-off of the (1,0) mode

Figure 4.36: Directivity plots for the large ALWA prototype operated by a dipole with the absorber termination

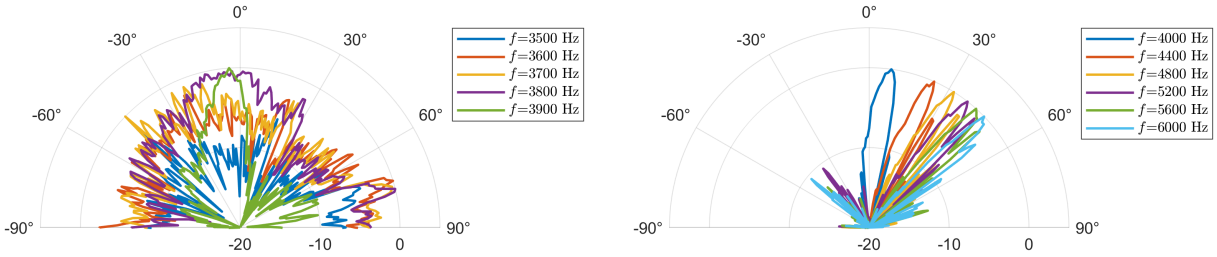

(a) Up to the cut-off of the (1,0) mode **(b)** Above the cut-off of the (1,0) mode

Figure 4.37: Directivity plots for the large ALWA prototype operated by a dipole with the reflector termination

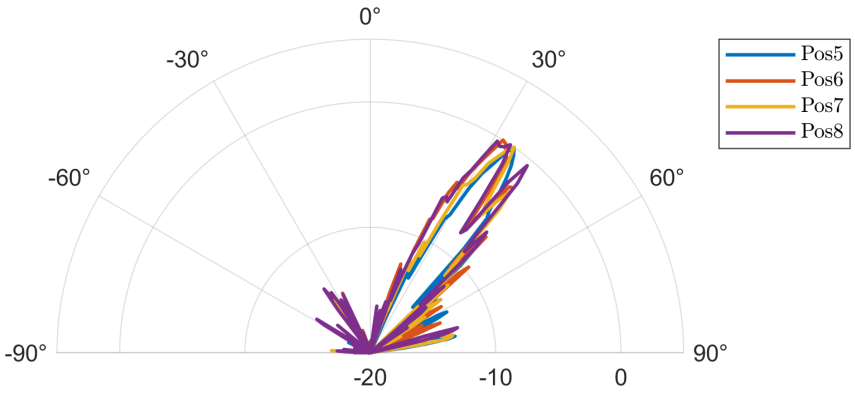

Figure 4.38: A polar plot of the directivity measured at different microphone positions for the small ALWA operated with a dipole source and an absorber termination.

4.6.3 Comparison of the Directivity from Comsol and from the Experimental Measurements

Figures 4.39 and 4.40 show a comparison of the directivity plots obtained from the Comsol simulations and from the experimental measurements with the absorber termination for the large antenna and the small antenna, respectively. Good agreement is observed for the large ALWA at 800 Hz with a monopole source (Figure 4.39a) and at 2500 Hz with a dipole source (Figure 4.39c). Good agreement is also seen for the small ALWA with a monopole source at 1500 Hz (Figure 4.40a).

For the large ALWA at 1000 Hz and the small ALWA at 2000 Hz with a monopole source (Figures 4.39b and 4.40b), it can be seen that the main lobe predicted by Comsol is present in the measurement, however, this is eclipsed by much stronger side or back lobes. These frequencies lie within the frequency range of the deviation which was measured for the respective antenna when operated with a monopole source.

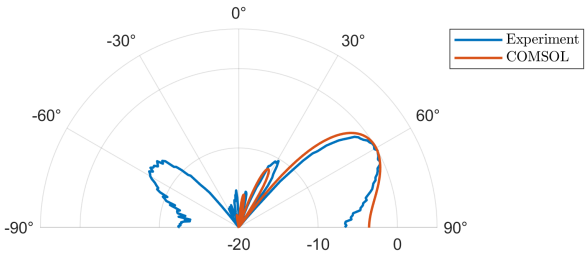

(a) Monopole source at 800 Hz

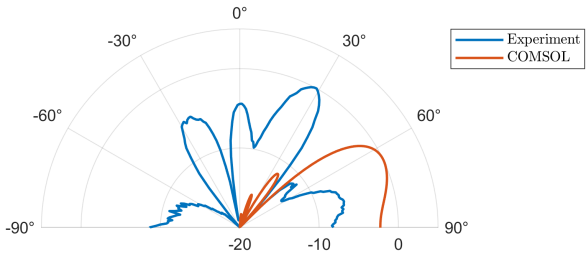

(b) Monopole source at 1000 Hz

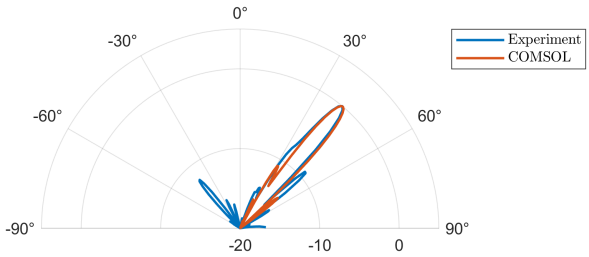

(c) Dipole source at 2500 Hz

Figure 4.39: Comparison of the measured directivity with the simulated directivity for the large ALWA prototype

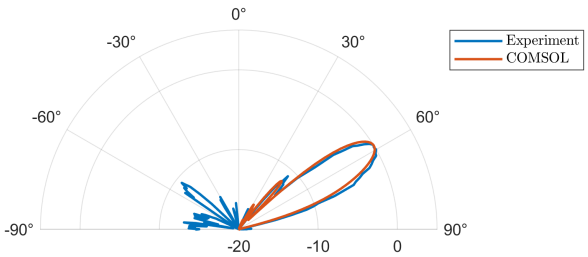

(a) Monopole source at 1500 Hz

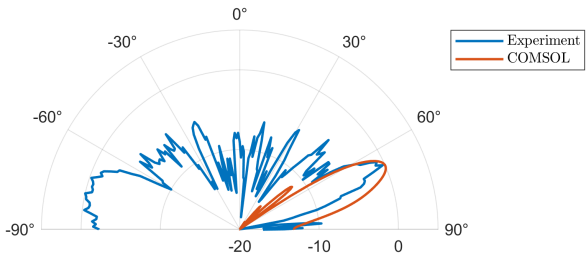

(b) Monopole source at 2000 Hz

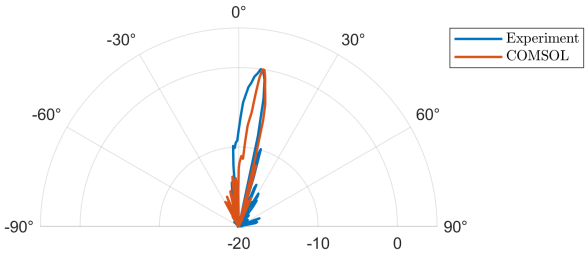

(c) Dipole source at 4000 Hz

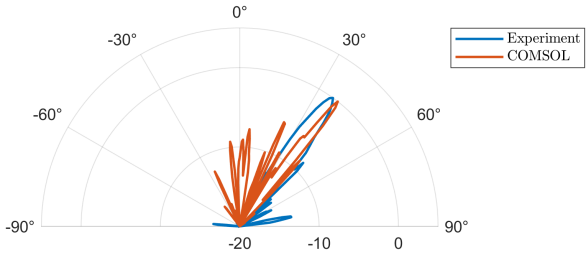

(d) Dipole source at 5000 Hz

Figure 4.40: Comparison of the measured directivity with the simulated directivity for the small ALWA prototype

In the case of the small ALWA operated with a dipole source at 5000 Hz (Figure 4.40d), a small offset can be seen between the measured directivity and the simulation. The side-lobes of the simulation are also a lot more prominent than in the measurement for this frequency. This may be due to errors in the construction of the model for this particular simulation. At 4000 Hz (Figure 4.40c), the offset is smaller and the side-lobes are less prominent in the simulation results than at 5000 Hz.

5

Conclusion

This chapter summarizes the findings of the study, including a brief description of the methods used and the results obtained. A discussion of the limitations of the study is presented, followed by future potential research topics based on the findings of this study.

5.1 Summary of the Method and Results

A theoretical model that describes the radiation angle and leakage factor of a rectangular natural material ALWA with either circular holes or a long slit as the radiating orifice was derived from fundamental principles and expressions for the impedance of different orifices from literature. This model was tested using FEM simulations in Comsol and by manufacturing a physical prototype for experimental measurements. Two modes of interest were identified from the theoretical model. Both modes have a cut-off frequency beyond which they start to radiate leaky waves. The (0,0) mode has a low cut-off frequency, while the (1,0) mode has a higher cut-off frequency. The (1,0) mode exhibits properties more suitable for applications which require the modulation of the design parameters along the length of the antenna. Compared to the (0,0) mode, the (1,0) mode shows a much larger shift in the cut-off frequency when changing the cavity width and a greater range of values for the leakage factor can be obtained by varying the dimensions of the radiating orifice.

Simulations were run for different dimensions of the radiating orifice, varying the slit height, the hole radius, and hole separation. Different types of sources were used to isolate the (1,0) mode from the (0,0) mode. Using a monopole source both modes are excited in for frequencies above their respective cut-off, however, the (0,0) mode dominates with this source type. Using a dipole mode, the excitation of the (0,0) mode is suppressed, allowing the (1,0) mode behavior to dominate. The results of the simulations showed good agreement with the theoretical model for the ALWA with circular holes for all of the dimensions tested. The results of the simulations for the slit ALWA showed worse but still satisfactory agreement.

The two designs of ALWAs with circular holes were chosen for experimental validation. The ALWA prototypes were manufactured from rectangular aluminum tubes and two loudspeakers were attached at one side using a 3D-printed fitting. The loudspeakers were operated in phase or with a 180° phase difference to create a monopole or dipole source,

respectively. At the other end of the antenna two different kinds of termination were used: an absorber and a reflector. Directivity measurements were made by placing the ALWA on a rotating table inside an anechoic chamber and exciting it with a sine sweep. Microphones were placed at different distances and initial angles from the ALWA to take repeated measurements. The directivity was calculated from the measured impulse responses as the absolute value of its Fourier Transform at fixed angles in steps of 1°.

The results of the experimental measurements demonstrated good agreement with the theoretical model and the FEM simulations. The measurements of the large ALWA prototype operated with a dipole source showed excellent results, matching the predicted radiation angle closely. The measurements of both the large and small ALWA prototypes operated with a monopole source showed good agreement but with a deviation at a frequency range around 1 kHz and 2 kHz respectively. It was hypothesized that this deviation was due to a resonance occurring along the width of the ALWA. The measurement of the small ALWA prototype operated with a dipole source appeared to be shifted from the theoretically predicted radiation angle. It was hypothesized that the cause of this shift was that the radiation was occurring at a point closer to the source, rather than effectively at the mid-point of the ALWA. This hypothesis was supported by comparing the directivity plots measured at different microphone positions.

5.2 Limitations of the Study

This study was limited by time constraints, which did not allow for more measurements to be made. It had originally been envisaged that the dimensions of the holes of the prototypes would be expanded to validate the model for a larger variety of parameters. It was also not possible to measure the slit ALWA due to manufacturing difficulties.

Additionally, some of the results presented in the parameter study were not validated by either simulations or measurements; particularly, the variation of the wall thickness and cavity height and width. While the curves shown in this section were not directly verified, the model was proven to work for both the small and large ALWA prototypes which had different combinations of values for these three parameters.

The theoretical model of the slit ALWA showed significant deviation from the simulated results in the (0,0) mode at frequencies close to and below the cut-off frequency. This suggests that some assumptions used to characterize the slit impedance are not valid in this regime. The theoretical model of the ALWA with circular holes, while providing good results, may also be improved by accounting for the phase and magnitude difference of the different holes when calculating the mutual impedance.

5.3 Future Research

Future research may be conducted using the theoretical model derived in this study to design modulated ALWAs with suppressed side-lobes for direction-finding applications. Other radiation patterns may also be designed using this model.

The absorber termination used for the physical prototypes did not completely suppress the back-lobes. The design of this termination could be improved, perhaps by using a wedge shaped absorber similar to the design used in anechoic chambers. The source could also be improved by analyzing the mode shapes of the pressure field inside the antenna to determine the optimal positioning of the loudspeakers for isolating the (1,0) mode from the (0,0) mode.

Furthermore, further research may be needed to identify the nature of the deviation from the theoretical model observed in the experimental measurements of the ALWAs operated with a monopole source.

Finally, a theoretical model for side-mounted Helmholtz resonators was derived and presented in Appendix A. If this model is validated with FEM simulations and experimental measurements, Helmholtz resonators may offer an additional parameter for modulation if the parameters considered in this study are not sufficient for some applications.

References

[1] C. J. Naify, M. Haberman, M. Guild, and C. Sieck, "Acoustic leaky wave antennas: Direction-finding via dispersion," *Acoust. Today*, vol. 14, no. 3, pp. 31–38, 2018.

[2] W. W. Hansen, *Radiating electromagnetic wave guide*, US Patent 2,402,622, Jun. 1946.

[3] D. R. Jackson and A. A. Oliner, "Leaky-wave antennas," in *Modern Antenna Handbook*. Wiley Telecom, 2008, pp. 325–367. DOI: 10.1002/9780470294154.ch7.

[4] D. R. Jackson, C. Caloz, and T. Itoh, "Leaky-wave antennas," *Proceedings of the IEEE*, vol. 100, no. 7, pp. 2194–2206, 2012. DOI: 10.1109/JPROC.2012.2187410.

[5] F. Bongard, H. Lissek, and J. R. Mosig, "Acoustic transmission line metamaterial with negative/zero/positive refractive index," *Phys. Rev. B*, vol. 82, p. 094 306, 9 Sep. 2010. DOI: 10.1103/PhysRevB.82.094306. [Online]. Available: https://link.aps.org/doi/10.1103/PhysRevB.82.094306.

[6] C. J. Naify, C. N. Layman, T. P. Martin, M. Nicholas, D. C. Calvo, and G. J. Orris, "Experimental realization of a variable index transmission line metamaterial as an acoustic leaky-wave antenna," *Applied Physics Letters*, vol. 102, no. 20, p. 203 508, May 2013, ISSN: 0003-6951. DOI: 10.1063/1.4807280. eprint: https://pubs.aip.org/aip/apl/article-pdf/doi/10.1063/1.4807280/14275248/203508_1_online.pdf. [Online]. Available: https://doi.org/10.1063/1.4807280.

[7] H. Esfahlani, S. Karkar, H. Lissek, and J. R. Mosig, "Acoustic dispersive prism," *Scientific reports*, vol. 6, no. 1, p. 18 911, 2016.

[8] H. Esfahlani, S. Karkar, H. Lissek, and J. R. Mosig, "Exploiting the leaky-wave properties of transmission-line metamaterials for single-microphone direction finding," *The Journal of the Acoustical Society of America*, vol. 139, no. 6, pp. 3259–3266, Jun. 2016, ISSN: 0001-4966. DOI: 10.1121/1.4949544. eprint: https://pubs.aip.org/asa/jasa/article-pdf/139/6/3259/15319718/3259_1_online.pdf. [Online]. Available: https://doi.org/10.1121/1.4949544.

[9] K. F. Woolfe, J. S. Rogers, M. D. Guild, and C. J. Naify, "Effect of waveguide impedance and sidelobe suppression on radiation beampatterns in underwater acoustic leaky wave antennas," in *OCEANS 2016 MTS/IEEE Monterey*, 2016, pp. 1–5. DOI: 10.1109/OCEANS.2016.7761394.

[10] C. W. Broadman, C. J. Naify, M. J. Lee, and M. R. Haberman, "Design of a one-dimensional underwater acoustic leaky wave antenna using an elastic metamaterial waveguide," *Journal of Applied Physics*, vol. 129, no. 19, p. 194 902, May 2021, ISSN: 0021-8979. DOI: 10.1063/5.0044802. eprint: https://pubs.aip.org/aip/jap/article-pdf/doi/10.1063/5.0044802/19766892/194902_1_online.pdf. [Online]. Available: https://doi.org/10.1063/5.0044802.

[11] L. E. Kinsler, A. R. Frey, A. B. Coppens, and J. V. Sanders, *Fundamentals of Acoustics (4th Edition)*. John Wiley & Sons, 1999, ISBN: 978-0-471-84789-2. [Online]. Available: https://app.knovel.com/hotlink/toc/id:kpFAE00003/fundamentals-acoustics/fundamentals-acoustics.

[12] A. Fernández-Garrido, M. Campo-Valera, E. Abdo-Sánchez, R. Picó, A.-J. Garcia-Sanchez, and R. Asorey-Cacheda, "Parametric study and experimental validation of acoustic leaky wave antenna in spatial localization," *IEEE Access*, vol. 13, pp. 10 371–10 385, 2025. DOI: 10.1109/ACCESS.2025.3528081.

[13] C. Caloz and T. Itoh, "Radiatedwave applications," in *Electromagnetic Metamaterials: Transmission Line Theory and Microwave Applications*. John Wiley & Sons, Inc., 2006, pp. 261–315. DOI: 10.1002/0471754323.ch6.

[14] M. Poveda-García, A. Algaba-Brazalez, and J. L. Gómez-Tornero, "Rigorous analysis of the different terms contributing to the attenuation constant in uniform leaky-wave antennas, under review," *IEEE Journal of Microwaves*, 2025.

[15] M. Poveda-García, A. Algaba-Brazalez, D. Comite, and J. L. Gómez-Tornero, "Impact of the reactive attenuation constant in the efficiency of uniform/quasi-uniform leaky-wave antennas radiating at broadside," in *2025 International Conference on Electromagnetics in Advanced Applications (ICEAA 2025)*, Palermo, Italy, Sep. 2025.

[16] I. Mann J. Adin, J. Tichy, and A. J. Romano, "Instantaneous and time-averaged energy transfer in acoustic fields," *The Journal of the Acoustical Society of America*, vol. 82, no. 1, pp. 17–30, Jul. 1987, ISSN: 0001-4966. DOI: 10.1121/1.395562. eprint: https://pubs.aip.org/asa/jasa/article-pdf/82/1/17/12215389/17_1_online.pdf. [Online]. Available: https://doi.org/10.1121/1.395562.

[17] E. Negri, W. Fuscaldo, P. Burghignoli, and A. Galli, "An overview of design techniques for two-dimensional leaky-wave antennas," *Applied Sciences*, vol. 15, no. 4, 2025, ISSN: 2076-3417. DOI: 10.3390/app15041854. [Online]. Available: https://www.mdpi.com/2076-3417/15/4/1854.

[18] The MathWorks Inc., *atan - Inverse tangent in radians*, Natick, Massachusetts, United States, 2022. [Online]. Available: https://se.mathworks.com/help/matlab/ref/double.atan.html.

[19] T. E. Vigran and O. K. Pettersen, "The absorption of slotted panels revisited," *Forum Acusticum Budapest 2005: 4th European Congress on Acustics*, pp. 2037–2040, 2005.

[20] T. E. Vigran, *Building acoustics*. CRC Press, 2008, p. 362, ISBN: 9780415428538.

[21] F. P. Mechel, "Radiation of sound," in *Formulas of Acoustics*. Berlin, Heidelberg: Springer Berlin Heidelberg, 2008, pp. 316–327, ISBN: 978-3-540-76833-3. DOI: 10.1007/978-3-540-76833-3_102. [Online]. Available: https://doi.org/10.1007/978-3-540-76833-3_102.

[22] W. Lauriks, J.-F. Allard, D. Lafarge, and G. Plantier, "Radiation impedance of an array of slits," *Acta Acustica united with Acustica*, vol. 80, pp. 87–89, 1994.

[23] T. E. Vigran, "The acoustic properties of panels with rectangular apertures," *The Journal of the Acoustical Society of America*, vol. 135, no. 5, pp. 2777–2784, May 2014, ISSN: 0001-4966. DOI: 10.1121/1.4871363. eprint: https://pubs.aip.org/asa/jasa/article-pdf/135/5/2777/8099281/2777_1_online.pdf. [Online]. Available: https://doi.org/10.1121/1.4871363.

[24] M. Kleiner, *Electroacoustics*. Taylor & Francis Group, 2013, ISBN: 9781466599437.

[25] R. T. Randeberg, "Perforated panel absorbers with viscous energy dissipation enhanced by orifice design," Ph.D. dissertation, Department of Telecommunications, Norwegian University of Science and Technology, 2000.

[26] R. L. Pritchard, "Mutual acoustic impedance between radiators in an infinite rigid plane," *The Journal of the Acoustical Society of America*, vol. 32, no. 6, pp. 730–737, Jun. 1960, ISSN: 0001-4966. DOI: 10.1121/1.1908199. eprint: https://pubs.aip.org/asa/jasa/article-pdf/32/6/730/18741832/730_1_online.pdf. [Online]. Available: https://doi.org/10.1121/1.1908199.

[27] H. Esfahlani, S. Karkar, H. Lissek, and J. R. Mosig, "Electromagnetic inspired acoustic leaky-wave antenna," in *2016 10th European Conference on Antennas and Propagation (EuCAP)*, 2016, pp. 1–4. DOI: 10.1109/EuCAP.2016.7481954.

[28] J. Lan, X. Peng, X. Zhang, X. Liu, and Y. Li, "Improving directional radiation quality based on a gradient amplitude acoustic leaky wave antenna," *New Journal of Physics*, vol. 21, no. 10, p. 103 023, 2019.

[29] J. L. Gomez-Tornero, A. R. Weily, and Y. J. Guo, "Rectilinear leaky-wave antennas with broad beam patterns using hybrid printed-circuit waveguides," *IEEE Transactions on Antennas and Propagation*, vol. 59, no. 11, pp. 3999–4007, 2011. DOI: 10.1109/TAP.2011.2164173.

[30] J. L. Gomez-Tornero, F. Quesada-Pereira, A. Alvarez-Melcon, G. Goussetis, A. R. Weily, and Y. J. Guo, "Frequency steerable two dimensional focusing using rectilinear leaky-wave lenses," *IEEE Transactions on Antennas and Propagation*, vol. 59, no. 2, pp. 407–415, 2011. DOI: 10.1109/TAP.2010.2096396.

[31] A. J. Martinez-Ros, J. L. Gómez-Tornero, and G. Goussetis, "Holographic pattern synthesis with modulated substrate integrated waveguide line-source leaky-wave antennas," *IEEE Transactions on Antennas and Propagation*, vol. 61, no. 7, pp. 3466–3474, 2013. DOI: 10.1109/TAP.2013.2257650.

[32] The MathWorks Inc., *fminsearch - Search for local minimum of unconstrained multivariable function using derivative-free method*, Natick, Massachusetts, United States, 2022. [Online]. Available: https://se.mathworks.com/help/matlab/ref/fminsearch.html.

[33] The MathWorks Inc., *Optimizing Nonlinear Functions*, Natick, Massachusetts, United States, 2022. [Online]. Available: https://se.mathworks.com/help/matlab/math/optimizing-nonlinear-functions.html#bsgpq6p-11.

[34] Comsol, *Perfectly matched boundary*. [Online]. Available: https://doc.comsol.com/6.0/doc/com.comsol.help.aco/aco_ug_pressure.05.035.html (visited on 06/04/2025).

[35] Comsol, *External field calculation*. [Online]. Available: https://doc.comsol.com/5.5/doc/com.comsol.help.aco/aco_ug_pressure.05.024.html (visited on 06/04/2025).

[36] Comsol, *Sound hard boundary*. [Online]. Available: https://doc.comsol.com/5.5/doc/com.comsol.help.aco/aco_ug_pressure.05.067.html (visited on 06/04/2025).

[37] S. Marburg, "Six boundary elements per wavelength: Is that enough?" *Journal of computational acoustics*, vol. 10, no. 01, pp. 25–51, 2002.

[38] G. Squires, *Practical Physics*. Cambridge, UK: Cambridge University Press, 2001, pp. 27–30.

[39] D. I. Havelock, S. Kuwano, and M. Vorländer, *Handbook of signal processing in acoustics*. Springer, 2008, vol. 1.

[40] S.-T. Yang and H. Ling, "Two-section half-width microstrip leaky wave antenna," *IEEE Transactions on Antennas and Propagation*, vol. 62, no. 10, pp. 4988–4996, 2014. DOI: 10.1109/TAP.2014.2345578.

[41] F. A. Morrison, *Uncertainty Analysis for Engineers and Scientists: A Practical Guide*. Cambridge, UK: Cambridge University Press, 2021, pp. 60–61.

A

Extending the Theoretical Model to Include a Helmholtz Resonator

The ALWA parameters can be altered by attaching a Helmholtz resonator on the opposite side of the radiating slit. The TRE for this design can be solved using a similar approach to the case for the rectangular ALWA without the Helmholtz resonator. In this case, the left wall is no longer rigid, so the TRE must be derived from Eq. (2.22) as:

$$\begin{aligned}
&\frac{Z_R + jZ_{0,x}\tan k_x W}{1 + j\frac{Z_R}{Z_{0,x}}\tan k_x W} = -Z_L \\
\implies & Z_R + jZ_{0,x}\tan k_x W = -Z_L\left[1 + j\frac{Z_R}{Z_{0,x}}\tan\left(k_x W\right)\right] \\
\implies & j\tan\left(k_x W\right)\left[Z_{0,x} + Z_L\frac{Z_R}{Z_{0,x}}\right] = -Z_L - Z_R \\
\implies & \tan\left(k_x W\right) = j\frac{Z_L + Z_R}{Z_{0,x} + Z_L\frac{Z_R}{Z_{0,x}}} \\
\implies & k_x = \frac{1}{W}\arctan\left[j\frac{Z_{0,x}\left(Z_L + Z_R\right)}{Z_{0,x}^2 + Z_R Z_L}\right].
\end{aligned} \tag{A.1}$$

Here, Z_L represents the impedance of the slit leading to the Helmholtz resonator, and Z_R represents the impedance of the radiating orifice. A negative sign is applied to Z_L since this faces in the opposite direction to Z_R.

The impedance of a long rectangular slit leading to a Helmholtz resonator can be written as [19]

$$Z_L = \frac{1}{\epsilon}(Z_{\mathrm{S}} + j\rho_0\omega 2\Delta d) - jZ_0\cot\left(h\frac{\omega}{c_0}\right). \tag{A.2}$$

Here Z_S and Δd are the surface impedance and end correction of the Helmholtz resonator slit and can be calculated for the dimensions of this slit using Eqs. (2.29) and (2.35), respectively. The geometry of the proposed ALWA with the Helmholtz resonator is defined in Figure A.1.

This model has not been validated using either FEM simulations or experimental measurements. Hence, this must first be done, identifying any errors in the model, before it can be applied to design ALWAs.

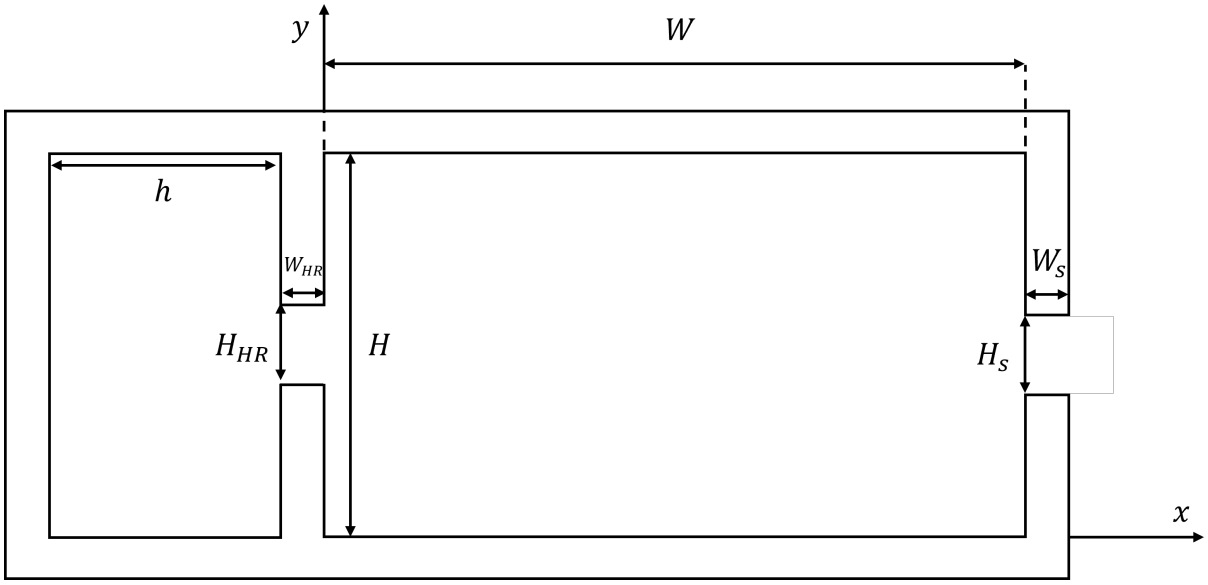

Figure A.1: Proposed geometry for an ALWA with a Helmholtz Resonator

DEPARTMENT OF SOME SUBJECT OR TECHNOLOGY
CHALMERS UNIVERSITY OF TECHNOLOGY
Gothenburg, Sweden
www.chalmers.se

CHALMERS
UNIVERSITY OF TECHNOLOGY